# IJIEA

## JOURNAL

### INTERNATIONAL JOURNAL OF INNOVATIVE ENGINEERING APPLICATIONS

**Editor-in-Chief**
Niyazi Özdemir
Hikmet Esen

**Deputy Editor-in-Chief**
Abdullah Kapıcıoğlu

**Managing Editor**
Cihangir Kale

#16
IJIEA

# IJIEA
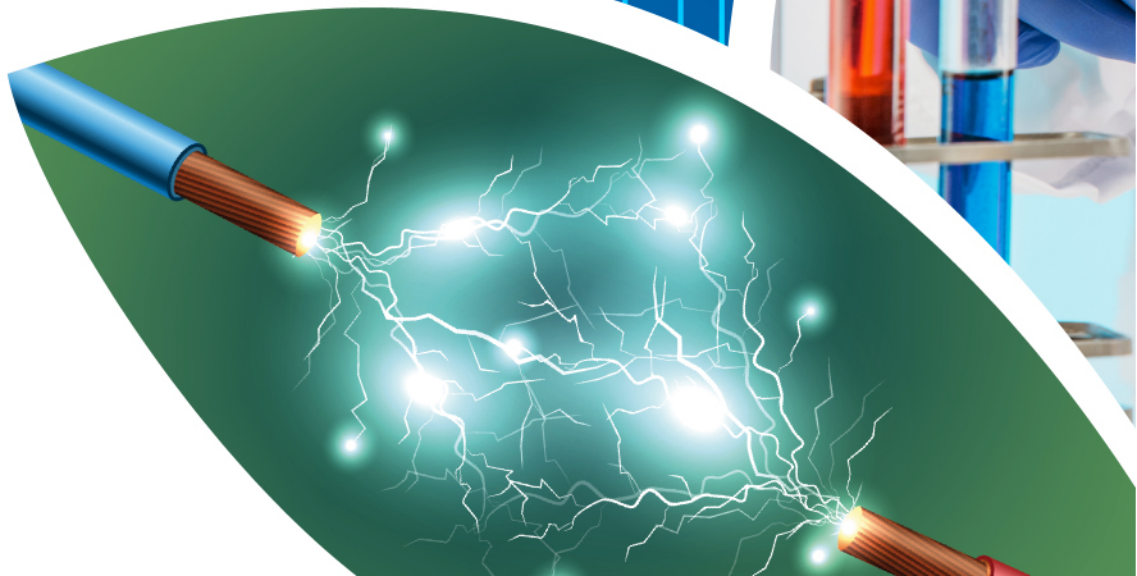# volume 8 issue 2
## CONTENTS / İÇİNDEKİLER

**International Journal of Innovative Engineering Applications**

Journal homepage: https://dergipark.org.tr/ijiea

# INVESTIGATION OF USAGE OPPORTUNITIES OF DIFFERENT PROPORTIONS OF WHEY AND CHIA SEED FLOUR IN BUTTERMILK

*Nilay Ozer[1]* iD *, Ozlem Pelin Can[*2]* iD

[1]*Sivas Cumhuriyet University, Faculty of Engineering, Department of Food Engineering, Sivas, Turkey*
[2]*Sivas Cumhuriyet University, Faculty of Veterinary Medicine, Department of Food Hygiene and Technology, Sivas, Turkey*

## *Abstract*

*Original scientific paper*

In this study, it was aimed to obtain a functional beverage with high nutritional value by using whey and chia seed flour in the production of ayran. In addition to its high nutritional value, while preventing whey from causing environmental pollution as a waste material, it is aimed to obtain a new dietary product with chia seed flour containing 34-40g fiber per 100g, antioxidant, omega-3 fatty acid and rich protein content. Experimental ayran samples were prepared by adding whey and chia seed flour at different rates. K (Ayran), $K_2$ (Ayran + 1% Chia seed flour), $K_3$ (Ayran + 0,5% Chia seed flour , Group 1(Ayran (75%) + Whey (25%) + 1% Chia seed flour), Group 2 (Ayran (75%) + Whey (25%) + 0,5% Chia seed flour), Group 3 (Ayran (50%) + Whey (50%) + 1% Chia seed flour), Group 4 (Ayran (50%) + Whey (50%) + 0,5% Chia seed flour) were kept at +4 ℃ and their physical, chemical and sensory properties were examined on the 1st, 3rd, 5th, 7th and 14th days. In the experimental ayran samples we researched, the use of whey and chia seed flour was found to have a significant effect on psychrophilic bacteria count (log cfu/ml), coliform group bacteria (log cfu/ml), yeast-mold count (log cfu/ml), lactobacil spp. (log cfu/ml) and lactococ spp. (log cfu/ml), pH, acidity (lactic acid), water-soluble dry matter (%), serum separation (%), color values (L*, a*, b*) and sensory properties (p<0,05). In this experimental study, when microbiological, physical, chemical and sensory analyzes are taken into account, the groups that can be used in ayran production were determined as the K2 and K3 groups containing Chia seed flour and the 1st group containing 25% Whey + %1 Chia seed flour. The use of the 3rd and 4th experimental groups was not possible. It has been identified that these experimentally determined rates can provide a new product to the functional food industry by enabling the use of whey and chia seed flour.

*Keywords: Ayran, chia seed, physical, chemical and sensory analyses, whey.*

## 1  Introduction

In our society, which is becoming increasingly conscious about healthy nutrition, the tendency towards functional foods is increasing day by day in order to use natural resources more efficiently. The low consumption habits of milk and dairy products, which have a great importance in human nutrition and are included in the animal food class, and the short shelf life have made it necessary to consume most of the milk as fermented milk products. Yoghurt and ayran are the leading fermented milk products. Ayran contains all the nutritional properties of yoghurt at different rates depending on the amount of water added [1].

The majority of the residual material in the dairy industry occurs in cheese production. 70-90% of the milk used in cheese making is separated as whey. Whey can become an environmentally harmful product if it is disposed into the environment due to the proteins and other nutrients in its composition [1]. The chemicals formed as a result of fermentation of the organic substances contained in the whey discharged into the environment cause environmental pollution and pose a

threat to living organisms [2]. In clinical studies, the use of whey in the treatment of cancer, AIDS, hepatitis B, cardiovascular diseases and osteoporosis has given successful results [3]. whey proteins are a superior source of essential amino acids than many proteins due to their biological properties and sulfur-containing amino acids such as cysteine and methionine. In the food industry, is added to many products such as confectionery, bakery products, meat products, soups, sauces, potato chips, snacks and various beverages [4,5].

Chia seed is a plant called *'Salvia hispanica* L.', which is used as food, medicine, cosmetics, perfumery and colouring matter [6]. Chia seed proteins have four different structures. These are globulin, albumin, gluten and prolamin. Globulin constitutes 52% of the total protein structure. The remaining part is shared equally by other proteins [7]. Approximately 1g of chia seed contains 0.75g of phenolic compounds such as chlorogenic acid, caffeic acid, quercetin and campferol in antioxidant structure. In addition, Chia seed, which is rich in calcium, phosphorus, potassium, magnesium, niacin, vitamin A and fibre content, is poor in sodium, iron, zinc and vitamin C [8]. Since 6% of Chia seed consists of soluble fibres,

products with high dietary fibre content can be obtained [9]. Chia seed is used as a thickener in the food industry because it can absorb 27 times its weight in water and form mucilage [10]. It has been observed that it contributes to the nutritional value by being used in the production of many bakery products, especially bread, in many food products such as biscuits, ice cream and animal feeds.

The aim of this study was to investigate the effects of ayran production with different ratios of whey and Chia seed flour on microbiological, chemical and sensory properties of ayran. It was aimed to prevent economic losses, prevent environmental pollution and increase the nutritional value of ayran by using whey, which is a waste material in dairy industry. In addition, the product quality and shelf life of a new functional food production was investigated by taking advantage of the antioxidant, dietary pulp and appetite control properties of Chia seed containing 34-40g fibre per 100g.

## 2 Material Method

### 2.1 Material

The ayran and whey were obtained from Sivas Cumhuriyet University Food Studies Application and Research Centre, Chia seeds were obtained from a commercial company, chemicals were obtained from TEKKİM (Istanbul, Turkey) and media were obtained from BİOCAR (Istanbul, Turkey).

### 2.2 Method

The raw milk was wheyteurised and then produced with the addition of starter culture considering the ayran production process. Whey obtained from white cheese production was wheyteurised at $65\,^{\circ}$C for 30 minutes and prepared for use. Chia seeds were ground into flour and then wheyteurised. The amount of chia seed flour and whey added was determined as a result of preliminary experiments and experimental samples were prepared. These are; K: Ayran (Control), K2: Ayran + 1% Chia seed flour, K3: Ayran + 0,5% Chia seed flour, 1: Ayran (75%) + whey (25%) + 1% Chia seed flour, 2: Ayran (75%) + whey (25%) + 0,5% Chia seed flour, 3: Ayran (50%) + whey (50%) + 1% Chia seed flour, 4: Ayran (50%) + whey (50%) + 0,5% Chia seed flour.
The prepared experimental samples were filled in the ayran filling machine, sealed and kept in cold storage at +4 $^{\circ}$C on the 1st, 3rd, 5th, 7th and 14th days to be investigated in terms of physical, chemical, microbiological and sensory properties.

### 2.2.1 Microbiological analyses

Experimental ayran samples were inoculated on Violet Red Bile Agar medium for coliform group bacteria enumeration using the pouring plate method. It was left to incubation at $37\,^{\circ}$C for 24 hours. For total psychrophilic bacteria group counting, Plate Count Agar medium was inoculated by pouring plate method. Colonies were counted by incubation at $6.5\,^{\circ}$C for 10 days. In the enumeration of lactic acid bacteria in experimental ayran samples, appropriate distillations were sown on Man Rogosa Sharpe Agar medium for Lactobacillus species and M17 Agar medium for Lactococus species by pouring plate method. After sowing, incubation was performed at $37\,^{\circ}$C for 48 hours. For total yeast and mould counts, Potato Dextrose Agar medium was sown by pouring plate method and colonies were counted by incubation at $25\,^{\circ}$C for 4-5 days [11].

### 2.2.2 Physical and Chemical Analyses

The pH values of the experimental ayran samples and whey were measured with a digital pH meter (HANNA HI 98128) [12]. Titration acidity was determined by titrimetric method [13]. The water soluble dry matter content of experimental ayran samples and whey was measured by digital refractometer (MİLWAUKEE MA871) [14]. For the determination of serum separation; 25 ml of experimental samples (at 4±1 $^{\circ}$C) were added to the filter paper placed in a tared funnel and kept for 120 minutes. The amount of serum filtered into the tared flask was weighed and multiplied by 4 and expressed as % [15]. Colour analysis of the experimental ayran samples was carried out by calorimeter (MINOLTA CR-400) using CIELAB colour method. This technique gives numerical values of three colour scales (L*, a*, b*) and L* indicates whiteness and brightness, a* indicates red and green, and b* indicates yellow and blue [16].

### 2.2.3 Sensory Analyses

The experimental ayran samples were analysed by 8 panelists. Water and crackers were offered between different sample analyses to prevent the flavours from being affected by each other. Appearance and texture, odour and taste characteristics were taken into consideration and evaluated on a scale of 1-10 [17].

### 2.2.4 Statistical Analyses

IBM SPSS 23.0 package programme was used to evaluate the data obtained in this study. The differences between the experimental sample groups were determined by One-Way Anova test to evaluate all analysis data and statistically significant differences were determined by Tukey HSD (Honestly Significant Difference) test. The differences of the experimental ayran samples between days were determined by General Linear Model- Repeated Measures analysis, which is a repeated measures analysis, and the differences obtained were determined by Bonferroni test [18].

## 3 Results and Discussion

### 3.1 Microbiological Analysis Results of Experimental Samples

According to the Turkish Food Codex Communiqué on Fermented Milk Products (Communiqué no: 2009/25), ayran should contain at least $10^6$ total specific microorganisms (cfu/ml) [19]. Except for yeast, which is used probiotic in ayran, it should be between $10^2$-$10^3$ in 2 out of 5 samples and less than $10^2$ in 3 samples. Mould

should be between $10^2$-$10^3$ in 2 out of 5 samples and less than $10^2$ in 3 samples, and E. coli and other pathogenic microorganisms should not be present [20]. Microbiological analysis findings of the experimental samples are given in Table 1.

The number of lactic acid bacteria in whey used in the experimental samples was determined as 1.01 log cfu/ml. Coliform bacteria and yeast-mould counts were found below the detectable value (< 10 cfu/ml).

In the experimental ayran samples, the number of coliform bacteria was found below the detectable level during storage. Bekiş (2019), found the number of coliform bacteria below the detectable level in his thesis study investigating the possibilities of using whey in kefir [17]. Ünalan (2022), stated that the number of coliform bacteria was below the detectable level in his thesis study investigating the possibilities of using different ratios of whey and mint oil in ayran [21]. Tamuçay-Özünlü and Koçak (2010) determined the number of coliform bacteria below the detectable level in their study in which they investigated the ayran quality of different heat treatment applications to milk [22].

Total psychrophilic bacteria counts of the experimental ayran samples were found in the range of 3.12-5.38 log cfu/ml. When the results of intra-group inter-day analyses of the experimental ayran samples during the storage period were examined, the difference between the K and K2 experimental ayran samples on the 1st and 3rd days and on the 5th, 7th and 14th days was found to be statistically significant ($p < 0.05$). When the experimental ayran samples were evaluated between groups during the storage period, the difference between the K3 and 1st groups on the 1st and 3rd days and between the K, K2, 2nd, 3rd and 4th groups was not found to be statistically significant ($p > 0.05$). When the results of the analysis were evaluated, the presence of whey and Chia seed flour did not affect the total number of psychrophilic bacteria due to the preparation of experimental samples by wheyteurising whey, ayran and Chia seed flour. It is thought that the existing differences are due to the packaging during the shelf life of ayran. Doğan (2022), in his study investigating the production of probiotic beverage by adding black cumin seed oil to whey and pomegranate juice mixture, stated that the total number of psychrophilic bacteria was in the range of 2.08-6.57 log cfu/ml [23]. Akarca and Tomar (2019), in their study on the chemical and microbiological properties of strained (pouch) yoghurt sold in the district markets of Afyonkarahisar province, stated that the total number of psychrophilic bacteria was found in the range of 2.50-4.39 log cfu/g [24]. Ünalan (2022) reported that the total number of psychrophilic bacteria was found in the range of 3.23-5.32 log cfu/ml in his thesis study in which he investigated the possibilities of using different ratios of whey and peppermint oil in ayran [21]. According to our research findings, the total number of psychrophile organisms was found close to these studies.

The number of lactobacil spp. was found to be in the range of 2.53-3.23 log cfu/ml during the storage period of the experimental ayran samples. The difference between the experimental ayran samples was found to be insignificant ($p > 0.05$). It is thought that the presence of

chia seed flour and whey did not affect the number of lactobacil spp.

Tulukoğlu (2019) found the number of Lactobacil spp. in the range of 8.70-13.11 log cfu/ml in a study investigating the use of whey in the production of Izmir tulum cheese [25]. Ünalan (2022) found the number of Lactobacil spp. in the range of 2.34-3.40 log cfu/ml in his thesis study investigating the possibilities of using different ratios of whey and mint oil in ayran [21]. Our research findings were close to the findings of Ünalan (2022) and lower than the findings of Tulukoğlu (2019) [21, 25]. The number of lactococ spp. in the experimental samples was found to be in the range of 2.70-3.53 log cfu/ml. The difference between the days within the group during the storage period was found to be statistically insignificant ($p > 0.05$). The difference between K, K2 and K3 groups was not statistically significant ($p > 0.05$). The difference between groups K2, K3 containing chia seed flour and groups 1, 2, 3, and 4 containing whey was statistically significant ($p < 0.05$). It is thought that the presence of whey decreased the number of lactococ spp. Tulukoğlu (2019), in a study investigating the use of whey culture in the production of Izmir tulum cheese, found the number of Lactococ spp. in the range of 6.77-10.46 log cfu/ml [25]. Dinç and Kahyaoğlu (2021), in their study on the examination of microbiological and physicochemical properties of commercial ayran, found that the number of Lactococ spp. number in the range of 2.12-3.66 log cfu/ml, Ünalan (2022) found the number of Lactococ spp. in the range of 2.59-4.15 log cfu/ml in his thesis study investigating the possibilities of using different ratios of whey and mint oil in separation [21, 26]. While our research findings were lower than the findings of Tulukoğlu (2019), they were close to the findings of Ünalan (2022) and Dinç and Kahyaoğlu (2021) [21, 25, 26].

In this study, the differences between the groups in yeast-mould count were not statistically significant ($p > 0.05$). The difference between days 1, 3 and 5, 7, 14 was found to be statistically significant ($p < 0.05$).

The results on days 5, 7 and 14 were found to be appropriate according to the Turkish Food Codex Communiqué on Fermented Milk Products (Communiqué No: 2009/25) [19]. Due to the wheyteurisation of the experimental ayran samples, it is thought that the yeast-mould count was below the detectable level on days 1 and 3. It is thought that whey and Chia seed flour do not affect the product quality negatively and the increase in yeast-mould count is related to shelf life.

Hayatoğlu (2021) determined the yeast-mould count in the range of 2.10-2.94 log cfu/ml in a study investigating the physical, chemical and microbiological properties of ayran produced with the addition of probiotic bacteria [27]. Akçay (2016) determined the yeast-mould count in the range of 2.36-4.71 log cfu/ml in a study on the production of spicy ayran and investigation of some of its properties [28]. Tamuçay-Özünlü and Koçak (2010), in their study in which they examined the effect of different heat treatment applications on ayran quality, stated that they found the yeast-mould count below the detectable level [22]. Çelik et al. (2016), in their study investigating the physicochemical and microbiological quality of yoghurt and ayran produced in Kırklareli, found the yeast-

mould count in the range of $2.3 \times 10^1$-$1.9 \times 10^5$ log cfu/ml and stated that it was above the limit value [29]. It was determined that our research findings were close to the findings of Akçay (2016) and different from the findings of other studies.

### 3.2 Chemical Analysis Results of Experimental Samples

Chemical analyses of the experimental samples are given in Table 2. Whey pH value was 6.31, % dry matter was 5.75 and titration acidity was 0.11 in terms of lactic acid.

L* value indicates whiteness and brightness. The results of within-group, between-day and between-group analyses of the experimental samples were found to be statistically significant (p<0.05). When the results between the groups were analysed, it was seen that the L* values of the 1st, 2nd, 3rd and 4th groups containing whey decreased compared to the K2, K3 groups containing K and Chia seed flour. In our study, it is thought that whey-containing samples reduce the brightness. Temen (2018), in a study investigating the production and some properties of quinoa flour-added ayran, L* value was reported in the range of 84.43-85.96 [29]. Ürkek et al. (2021), in a study investigating the effect of chia addition on the physicochemical and sensory properties of ice cream, reported that they found the L* value in the range of 58.98-80.30 [30]. While our research findings were close to the findings of Temen (2018), they were higher than the findings of Ürkek et al. (2021) [29, 30]. Because, our study was used whey.

When the results of the analysis between the groups were evaluated, it was determined that the a* value of the 1st, 2nd, 3rd and 4th samples containing whey was lower than the K, K2 and K3 groups. Since whey is a yellowish-green coloured organic liquid, it is seen that the greenness value increases as the whey ratio increases. It is thought that chia seed flour adversely affects the homogeneous distribution due to its particulate structure and makes a difference in the findings during storage. Temen (2018) determined the a* value in the range of -2.92 to -2.67 in a study investigating the production and some properties of ayran with quinoa flour addition [29]. Ürkek et al. (2021) reported the a* value in the range of -2.86 to 1.54 in a study investigating the effect of chia addition on the physicochemical and sensory properties of ice cream [30]. It was determined that our research findings were not close to these studies.

When the b* value is evaluated between the groups, the b* value increases in groups 1, 2, 3 and 4 containing whey compared to K2 and K3 groups containing K and Chia seed flour (p<0.05). It is thought that the whey ratio increases the yellowness. Temen (2018), in a study investigating the production and some properties of quinoa flour-added ayran, determined the b* value in the range of 7.49 to 7.90 [29]. Ürkek et al. (2021), in a study investigating the effect of chia addition on the physicochemical and sensory properties of ice cream, determined the b* value in the range of 0.31-6.81. It was determined that our research findings were not close to these studies [30].

When the experimental samples were evaluated in terms of pH and titration acidity, the statistical difference was found to be insignificant (p>0.05, table 2). pH value was determined between 4.05 and 4.78. Titration acidity was determined insignificant when statistical analyzis (Table 2).

When the water soluble dry matter values of the experimental ayran samples were analysed during the storage period, it was found that the water soluble dry matter value increased as the % whey ratio increased and this is thought to be due to the high dry matter content of whey.

When the serum separation values of the samples during the preservation period were compared with the 1st, 2nd, 3rd and 4th groups and K, K2 and K3 groups, the difference was found to be statistically significant (p<0.05). It was determined that the presence of whey increased the serum separation value.

### 3.3 Sensory Analysis Results of Experimental Samples

The sensory analysis findings of the experimental samples are given in Table 3. When the samples were analysed in terms of appearance, the highest score was obtained by group K3 and the lowest score was obtained by group 3 containing 50% whey. It was observed that the homogenous appearance decreased as the storage time and whey amount increased. K2 and K3 groups received the highest score in the pleasant and distinctive odour parameter during the storage period. 3rd and 4th groups containing 50% whey received the lowest score. It is thought that there is a decrease in pleasant odour due to the increase in whey ratio. During the storage period of the experimental ayran samples, the highest score for the pleasant and distinctive flavour parameter was obtained by the K2 group and the lowest score was obtained by the 4th group. It is thought that the taste of the panellists decreased with the increase in sour taste as the storage time and whey amount increased. In terms of sensory analyses, it was determined that K2 and K3 groups received the highest score by the panelists during the storage period. It is thought that chia seed flour provided sufficient flavour and consistency among the reasons why K3 group was liked. Among the experimental ayran groups prepared with whey, it was determined that the 3rd and 4th groups received the lowest scores in all parameters. The increase in acidity and serum separation during storage shortens the shelf life of ayran. The reason for the 3rd and 4th experimental groups to get the lowest score is thought to be that whey accelerates acid formation. Bekiş (2019), in his study investigating the possibilities of using whey in kefir, stated that the homogeneous and foamy structure was lost in the last days of storage, the viscosity decreased and the appearance characteristics were less liked by the panellists due to reasons such as serum separation [17].

In this study we conducted, microbiological, physical, chemical and considering the sensory analyses, it may be possible to use in milk production. Groups K2 and K3 containing Chia seed flour and 25% Whey + 10 g Chia seeds. It was determined as the 1st group containing flour. These experimentally determined rates functional food by allowing the use of whey and chia seed flour. It has been determined that it can bring a new product to the industry.

**Table 1.** Microbiological analysis results of experimental ayran samples.

| Analysis | Groups | Storage time (days) | | | | |
|---|---|---|---|---|---|---|
| | | 1 | 3 | 5 | 7 | 14 |
| TPAB | K | 4,52±0,01[bA] | 4,68±0,02[bA] | 5,31±0,02[cB] | 5,34±0,03[bB] | 5,38±0,10[aB] |
| | K2 | 4,28±0,02[bA] | 4,32±0,01[bA] | 4,93±0,02[bB] | 5,12±0,08[bB] | 5,13±0,05[aB] |
| | K3 | 3,12±0,02[aA] | 3,47±0,03[aA] | 3,77±0,14[aA] | 5,04±0,07[bB] | 5,21±0,18[aB] |
| | 1 | 3,56±0,02[aA] | 3,83±0,02[aA] | 4,45±0,07[bB] | 5,04±0,08[bC] | 5,07±0,05[aC] |
| | 2 | 4,42±0,02[bA] | 4,73±0,03[bA] | 5,24±0,02[cB] | 4,88±0,01[aA] | 5,15±0,30[aB] |
| | 3 | 4,08±0,01[bA] | 4,66±0,02[bB] | 5,17±0,02[cC] | 5,03±0,03[bC] | 5,09±0,08[aC] |
| | 4 | 4,35±0,02[bA] | 4,92±0,02[bB] | 5,00±0,08[cB] | 5,03±0,04[bB] | 5,07±0,03[aB] |
| *Lactobacil* | K | 3,23±0,01 | 3,15±0,01 | 2,92±0,01 | 3,06±0,01 | 2,89±0,02 |
| | K2 | 2,85±0,02 | 2,76±0,05 | 2,69±0,01 | 2,68±0,02 | 2,79±0,01 |
| | K3 | 2,87±0,03 | 2,78±0,02 | 2,68±0,01 | 2,71±0,02 | 2,81±0,01 |
| | 1 | 2,83±0,01 | 2,77±0,01 | 2,69±0,02 | 2,65±0,02 | 2,90±0,01 |
| | 2 | 2,93±0,01 | 2,83±0,01 | 2,79±0,01 | 2,67±0,02 | 2,90±0,01 |
| | 3 | 2,72±0,01 | 2,77±0,06 | 2,84±0,01 | 2,53±0,01 | 2,88±0,01 |
| | 4 | 2,73±0,02 | 2,92±0,01 | 2,67±0,01 | 2,65±0,02 | 2,90±0,01 |
| *Lactococ* | K | 3,53±0,01[b] | 3,51±0,01[b] | 3,19±0,01[b] | 3,25±0,01[b] | 3,11±0,01[b] |
| | K2 | 3,08±0,02[b] | 2,83±0,01[a] | 2,79±0,02[a] | 2,86±0,01[a] | 3,23±0,01[b] |
| | K3 | 3,06±0,01[b] | 2,82±0,01[a] | 2,78±0,02[a] | 2,90±0,01[a] | 3,21±0,01[b] |
| | 1 | 2,77±0,13[a] | 2,78±0,02[a] | 2,80±0,04[a] | 2,82±0,02[a] | 2,90±0,02[a] |
| | 2 | 2,77±0,10[a] | 2,78±0,27[a] | 2,70±0,12[a] | 2,71±0,12[a] | 2,85±0,03[a] |
| | 3 | 2,81±0,02[a] | 2,79±0,01[a] | 2,79±0,01[a] | 2,78±0,01[a] | 2,91±0,01[a] |
| | 4 | 2,92±0,01[a] | 2,90±0,02[a] | 2,85±0,01[a] | 2,79±0,01[a] | 2,91±0,01[a] |
| Mould-yeast | K | <1 | <1 | 4,30±0,01 | 4,40±0,01 | 4,65±0,02 |
| | K2 | <1 | <1 | 4,33±0,03 | 4,75±0,02 | 4,96±0,02 |
| | K3 | <1 | <1 | 4,18±0,02 | 4,54±0,03 | 4,63±0,28 |
| | 1 | <1 | <1 | 4,49±0,02 | 4,73±0,06 | 4,86±0,04 |
| | 2 | <1 | <1 | 4,43±0,02 | 4,52±0,02 | 4,83±0,01 |
| | 3 | <1 | <1 | 4,32±0,01 | 4,61±0,02 | 4,74±0,01 |
| | 4 | <1 | <1 | 4,26±0,02 | 4,48±0,01 | 4,62±0,02 |

**K:Control, K2: Ayran + 1% Chia seed flour, K3: Ayran + 0,5% Chia seed flour, 1: Ayran (75%) + WHEY (25%) + 1% Chia seed flour, 2: Ayran (75%) + WHEY (25%) + 0,5% Chia seed flour, 3: Ayran (50%) + WHEY (50%) + 1% Chia seed flour, 4: Ayran (50%) + WHEY (50%) + 0,5% Chia seed flour.
a-g: The difference between samples with different letters in the same column is significant (p<0,05). A-C: The difference between samples with different letters in the same line is significant (p<0,05). The not difference between samples with different letters in the same line is insignificant and not determinad (p>0,05)

**Table 2.** Chemical analysis results of experimental ayran samples.

| Analysis | Groups | Storage time (days) | | | | |
|---|---|---|---|---|---|---|
| | | 1 | 3 | 5 | 7 | 14 |
| *L* value | K | 91,26±0,68[eA] | 92,76±0,34[cB] | 94,75±0,58[cC] | 97,16±0,19[dD] | 98,95±1,20[cE] |
| | K2 | 90,86±1,46[dA] | 93,35±0,11[dB] | 94,98±0,54[cC] | 96,03±0,25[cD] | 98,31±0,02[cE] |
| | K3 | 91,79±0,05[eA] | 93,49±0,54[eB] | 96,82±0,49[dC] | 98,39±0,02[eD] | 99,57±0,12[dE] |
| | 1 | 87,95±0,06[bA] | 90,86±0,55[bB] | 92,58±0,72[bC] | 94,63±0,12[bD] | 96,12±0,22[bE] |
| | 2 | 88,71±0,02[cA] | 90,56±0,80[bB] | 92,68±0,93[bC] | 94,35±1,13[bD] | 96,60±0,09[bE] |
| | 3 | 86,22±0,10[aA] | 88,98±0,54[aB] | 90,87±0,75[aC] | 93,73±0,11[aD] | 96,58±0,30[bE] |
| | 4 | 86,35±0,09[aA] | 88,69±1,41[aB] | 90,31±1,22[aC] | 93,55±1,45[aD] | 95,08±0,45[aE] |
| *a* value | K | -0,60±0,01[bA] | -0,76±0,01[bA] | -0,82±0,09[bA] | -0,96±0,03[bA] | -2,87±0,09[aB] |
| | K1 | -0,48±0,03[bA] | -1,80±0,02[cB] | -1,86±0,10[cB] | -1,92±0,03[cB] | -3,51±0,10[aC] |
| | K2 | -0,40±0,03[bA] | -1,16±0,02[cB] | -1,29±0,12[cB] | -1,51±0,01[cB] | -3,11±0,12[aC] |
| | 1 | -1,10±0,02[aA] | -2,10±0,01[aB] | -2,63±0,14[aB] | -2,69±0,03[aB] | -3,22±0,26[aC] |
| | 2 | -1,18±0,02[aA] | -2,30±0,01[aB] | -2,42±0,05[aB] | -2,65±1,19[aB] | -3,34±0,15[aC] |
| | 3 | -1,77±0,06[aA] | -2,58±0,05[aB] | -2,76±0,09[aB] | -2,82±0,04[aB] | -3,80±0,46[aC] |
| | 4 | -1,98±0,05[aA] | -2,78±0,02[aB] | -2,92±0,09[aB] | -2,95±0,16[aB] | -3,95±0,75[aC] |
| *b* value | K | 3,89±0,09[aE] | 2,75±0,06[aD] | 1,61±0,08[aC] | 0,26±0,11[aB] | -2,31±0,05[bA] |
| | K1 | 4,94±0,04[bE] | 3,82±0,07[bD] | 2,06±0,32[bC] | 0,68±0,01[aB] | -2,95±0,09[bA] |
| | K2 | 4,86±0,02[bE] | 3,77±0,14[bD] | 2,59±0,07[bC] | 1,09±0,01[bB] | -2,81±0,19[bA] |
| | 1 | 5,03±0,03[cE] | 3,96±0,32[bD] | 2,85±0,08[bC] | 1,20±0,08[bB] | -3,44±0,38[sA] |
| | 2 | 5,01±0,05[cD] | 3,61±0,69[bC] | 2,99±0,10[bB] | 2,27±0,59[cB] | -3,91±0,35[sA] |
| | 3 | 5,13±0,04[cE] | 4,88±0,14[cD] | 3,17±0,59[cC] | 1,80±0,08[cB] | -3,40±0,14[aA] |
| | 4 | 5,25±0,02[cE] | 4,58±0,04[cD] | 3,79±0,17[cC] | 1,85±0,59[cB] | -3,63±0,09[aA] |
| pH | K | 4,18±0,00 | 4,09±0,00 | 4,11±0,00 | 4,10±0,00 | 4,05±0,01 |
| | K1 | 4,17±0,00 | 4,13±0,00 | 4,11±0,01 | 4,09±0,00 | 4,05±0,00 |
| | K2 | 4,16±0,01 | 4,12±0,00 | 4,07±0,00 | 4,07±0,00 | 4,05±0,00 |
| | 1 | 4,40±0,00 | 4,31±0,00 | 4,26±0,00 | 4,33±0,01 | 4,45±0,00 |
| | 2 | 4,41±0,01 | 4,28±0,01 | 4,27±0,01 | 4,21±0,01 | 4,23±0,01 |
| | 3 | 4,78±0,00 | 4,59±0,00 | 4,46±0,00 | 4,58±0,00 | 4,55±0,00 |
| | 4 | 4,76±0,00 | 4,58±0,01 | 4,48±0,00 | 4,52±0,01 | 4,54±0,01 |

**Table 2 (Continued).** Chemical analysis results of experimental ayran samples.

| Analysis | Group | | | | | |
|---|---|---|---|---|---|---|
| Acidity | K | 0,49±0,001 | 0,54±0,003 | 0,46±0,001 | 0,51±0,001 | 0,45±0,080 |
| | K1 | 0,47±0,002 | 0,46±0,001 | 0,43±0,001 | 0,47±0,002 | 0,47±0,010 |
| | K2 | 0,46±0,001 | 0,45±0,011 | 0,41±0,002 | 0,48±0,000 | 0,41±0,030 |
| | 1 | 0,57±0,001 | 0,57±0,001 | 0,50±0,000 | 0,55±0,001 | 0,59±0,120 |
| | 2 | 0,53±0,001 | 0,55±0,004 | 0,51±0,010 | 0,59±0,002 | 0,56±0,080 |
| | 3 | 0,62±0,001 | 0,63±0,001 | 0,64±0,001 | 0,66±0,000 | 0,65±0,130 |
| | 4 | 0,61±0,001 | 0,64±0,000 | 0,60±0,001 | 0,62±0,000 | 0,64±0,050 |
| Dry matter | K | $2,25\pm0,00^{aB}$ | $2,63\pm0,04^{aB}$ | $2,20\pm0,00^{aB}$ | $1,07\pm0,02^{aA}$ | $0,96\pm0,01^{aA}$ |
| | K1 | $3,93\pm1,03^{bC}$ | $3,82\pm0,00^{bC}$ | $2,76\pm0,04^{aB}$ | $2,23\pm0,01^{bB}$ | $0,88\pm0,11^{aA}$ |
| | K2 | $3,88\pm0,04^{bB}$ | $3,20\pm0,10^{bB}$ | $3,18\pm0,04^{bB}$ | $2,53\pm0,11^{bA}$ | $2,53\pm0,04^{bA}$ |
| | 1 | $3,80\pm0,00^{bB}$ | $3,88\pm0,74^{bB}$ | $3,60\pm0,10^{bB}$ | $3,08\pm0,04^{cB}$ | $2,60\pm0,00^{bA}$ |
| | 2 | $3,88\pm0,01^{bB}$ | $3,86\pm0,04^{bB}$ | $3,85\pm0,04^{bB}$ | $3,50\pm0,64^{cB}$ | $2,65\pm0,00^{bA}$ |
| | 3 | $3,96\pm0,01^{bA}$ | $3,93\pm0,04^{bA}$ | $3,80\pm0,00^{bA}$ | $3,76\pm0,01^{cA}$ | $3,70\pm0,07^{cA}$ |
| | 4 | $4,80\pm0,01^{cB}$ | $4,46\pm0,10^{cB}$ | $3,73\pm0,05^{bA}$ | $3,38\pm0,74^{cA}$ | $3,34\pm0,04^{cA}$ |
| Serum seperation | K | $69,63\pm2,02^{bA}$ | $70,65\pm0,10^{bA}$ | $70,15\pm0,10^{bA}$ | $71,40\pm0,00^{cA}$ | $72,83\pm0,00^{dA}$ |
| | K1 | $66,22\pm0,00^{aB}$ | $66,18\pm0,01^{aB}$ | $66,03\pm0,04^{aB}$ | $66,45\pm0,10^{aB}$ | $64,25\pm0,10^{aA}$ |
| | K2 | $67,41\pm0,11^{aB}$ | $66,89\pm0,04^{aB}$ | $66,78\pm0,04^{aB}$ | $66,63\pm0,04^{aB}$ | $65,40\pm0,00a^{A}$ |
| | 1 | $68,21\pm0,04^{aC}$ | $67,66\pm0,02^{aC}$ | $66,23\pm0,04^{aB}$ | $66,81\pm0,01^{aB}$ | $64,70\pm0,42^{aA}$ |
| | 2 | $73,13\pm0,11^{dC}$ | $72,45\pm0,35^{cC}$ | $71,98\pm0,04^{cB}$ | $71,86\pm0,10^{cB}$ | $70,68\pm0,11^{cA}$ |
| | 3 | $71,00\pm0,00^{cC}$ | $70,58\pm0,11^{bC}$ | $69,45\pm0,10^{bB}$ | $69,41\pm0,01^{bB}$ | $68,00\pm0,00^{bA}$ |
| | 4 | $75,20\pm0,00^{eC}$ | $74,03\pm0,04^{dC}$ | $73,80\pm0,00^{dB}$ | $73,52\pm0,04^{dB}$ | $72,48\pm0,95^{dA}$ |

\*\*K:Control, K2: Ayran + 1% Chia seed flour, K3: Ayran + 0,5% Chia seed flour, 1: Ayran (75%) + WHEY (25%) + 1% Chia seed flour, 2: Ayran (75%) + WHEY (25%) + 0,5% Chia seed flour, 3: Ayran (50%) + WHEY (50%) + 1% Chia seed flour, 4: Ayran (50%) + WHEY (50%) + 0,5% Chia seed flour.
a-g: The difference between samples with different letters in the same column is significant ($p<0,05$). A-C: The difference between samples with different letters in the same line is significant ($p<0,05$). The not difference between samples with different letters in the same line is insignificant and not determinad ($p>0,05$)

**Table 3.** Sensory analysis total score results of experimental ayran samples.

| Analysis | Groups | | | | | | |
|---|---|---|---|---|---|---|---|
| | K | K2 | K3 | 1 | 2 | 3 | 4 |
| Homogeneity | 45,94 | 37,18 | 37,18 | 37,18 | 37,18 | 37,18 | 37,18 |
| Colour | 45,56 | 45,56 | 45,56 | 45,56 | 45,56 | 45,56 | 45,56 |
| Saturation | 38,94 | 38,94 | 38,94 | 38,94 | 38,94 | 38,94 | 38,94 |
| Vizkozity | 37,82 | 37,82 | 37,82 | 37,82 | 37,82 | 37,82 | 37,82 |
| Serum Seperation | 17,19 | 17,19 | 17,19 | 17,19 | 17,19 | 17,19 | 17,19 |
| Odour | 34,44 | 34,44 | 34,44 | 34,44 | 34,44 | 34,44 | 34,44 |

\*\*K:Control, K2: Ayran + 1% Chia seed flour, K3: Ayran + 0,5% Chia seed flour, 1: Ayran (75%) + WHEY (25%) + 1% Chia seed flour, 2: Ayran (75%) + WHEY (25%) + 0,5% Chia seed flour, 3: Ayran (50%) + WHEY (50%) + 1% Chia seed flour, 4: Ayran (50%) + WHEY (50%) + 0,5% Chia seed flour.
a-g: The difference between samples with different letters in the same column is significant ($p<0,05$). A-C: The difference between samples with different letters in the same line is significant ($p<0,05$).

## Declaration

Ethics committee approval is not required.

## References

[1] Carvolho, F., Prazeres, A. R., & Rivas, J. (2013). Cheese Whey Wastewater: Characterization and Treatment. *Science of the Total Environment, 445,* 385–396.

[2] Kurt, A. (1990). *Süt Teknolojisi.* Atatürk Üniversitesi Yayınları, 397–399s, Erzurum

[3] Marshall, K. (2004). Therapeutic Applications of Whey Protein. *Alternative Medicine Review, 9,* 136–156s.

[4] Küçüköner, E. (2011). Peynir Tozu ve Peynir Altı Suyu Tozu Üretimi. *1. Ulusal Helal ve Sağlıklı Gıda Kongresi,* 19–20 Kasım, Ankara.

[5] Yüksel, N., Muti İstek, M., & Bulca, S. (2020). Peynir Altı Suyu Proteinlerinin Gıda Ambalajlamada Film ve Kaplama Materyali Olarak Kullanımı. *Iğdır Üniversitesi Fen Bilimleri Enstitüsü Dergisi, 10(2),* 1042–1052.

[6] Çetin Karakaş, C. (2021). *Chia Tohumunun (Salvia Hispanica L.) Ratlarda Kafeterya Diyeti ile İndüklenen Obezite Üzerine Etkisi* (Doctoral Dissertation, Hacettepe University)

[7] Ergene, E., & Bingöl, E. B. (2019). Diyet Lif İçeriği Yüksek Bazı Gıdalar ve Beslenme Üzerine Etkileri. *Adnan Menderes Üniversitesi Sağlık Bilimleri Fakültesi Dergisi, 3(1),* 70–78s.

[8] Çelikoğlu, O. (2019). *Chia Tohumunun Broyler Piliçlerin Besi Performansı ve Et Raf Ömrüne Etkisi* (Master's Dissertation, Mehmet Akif Ersoy University).

[9] Goh, K. K. T., Matia-Merino, L., Chiang, J. H., Quek, R., Soh, S. J. B., & Lentle, R. G. (2016). The Physico-Chemical Properties of Chia Seed Polysaccharide and Its Microgel Dispersion Rheology. *Carbohydrate, 149,* 297–307.

[10] Erdoğdu, M. (2019). *Chia (Salvia Hispanica L.) Tohumu İlave Edilmiş Köftelerin Fizikokimyasal Özelliklerinin Belirlenmesi* (Master's Dissertation, Namık Kemal University).

[11] Halkman, A. K. (2005). *Merck Gıda Mikrobiyolojisi Uygulamaları.* 1. Baskı. Başak Matbaacılık, Ankara.

[12] Kurt, A., Çakmakçı, S., & Çağlar, A. (2003). *Süt ve Mamülleri Muayene ve Analiz Metotları Rehberi,* Genişletilmiş 8. Baskı. Atatürk Üniversitesi Ziraat Fakültesi Yayınları No:252/D, 73s, Erzurum.

[13] Türk Standartları Enstitüsü. (2002). TS 1018, Çiğ İnek Sütü Standardı. Ankara: Türk Standartları Enstitüsü

[14] Bal, E., & Çelik, S. (2008). Hasat Sonrası UV-C Uygulamalarının Giant Erik Çeşidinin Meyve Kalitesi ve Soğukta Muhafazası Üzerine Etkileri. *Ankara Üniversitesi Ziraat Fakültesi Tarım Bilimleri Dergisi, 14(2),* 101–107.

[15] İpin, G. F. (2011). *Krema Yoğurdunun Özellikleri Üzerine Süt Tozu İlavesi ve Depolama Süresinin Etkileri* (Master's Dissertation, Çukurova University).

[16] Okur, Ö. D., & Güzel-Seydim, Z. (2011). Geleneksel Dolaz Peynirinde Bazı Karakteristik Özelliklerin Belirlenmesi. *Ege Üniversitesi Ziraat Fakültesi Dergisi, 48(2),* 113–117.

[17] Bekiş, P. (2019). *Peynir Altı Suyunun Kefirde Kullanım Olanaklarının Araştırılması* (Master's Dissertation, Sivas Cumhuriyet University).

[18] Hastaoğlu, E. (2019). *Doğal Esansiyel Yağlar ve Doğal Ekstraktlar ile Emülsifiye Et Ürünleri Üretimi ve Kalite Özelliklerinin İncelenmesi* (Doctoral Dissertation, Hacettepe University).

[19] Tarım ve Köy İşleri Bakanlığı. (2009). *Türk Gıda Kodeksi Fermente Süt Ürünleri Tebliği (2009/25).*

[20] FAO/WHO. (2001). *Codex Standard for Fermented Milks.* (Codex Stan 243). Rome: FAO/WHO.

[21] Ünalan, Ş. M. (2022). *Farklı Oranlarda Peynir Altı Suyu ve Nane Yağının Ayranda Kullanım Olanakları* (Master's Dissertation, Cumhuriyet University).

[22] Tamuçay Özünlü, B., & Koçak, C. (2010). Süte Farklı Isıl İşlem Uygulamalarının Ayran Kalitesine Etkisi. *Gıda, 35(5),* 355–362.

[23] Doğan, B. (2022). *Peynir Altı Suyu ve Nar Suyu Karışımına Çörek Otu Yağı Katılarak Probiyotik İçecek Üretimi* (Master's Dissertation, Mehmet Akif Ersoy University).

[24] Akarca, G., & Tomar, O. (2019). Afyonkarahisar İli Semt Pazarlarında Satılan Süzme (Kese) Yoğurtların Kimyasal ve Mikrobiyolojik Özellikleri. *Akademik Gıda Dergisi, 17(2),* 212–216.

[25] Tulukoğlu, G. B. (2019). *İzmir Tulum Peyniri Yapımında Peynir Altı Suyu (Whey) Kültürünün Kullanımı* (Master's Dissertation, Ege University).

[26] Dinç, B. H., & Kahyaoğlu, D. (2021). Kastamonu'da Tüketilen Ticari Ayranların Bazı Mikrobiyolojik ve Fizikokimyasal Özelliklerinin İncelenmesi. *Süleyman Demirel Üniversitesi Fen Bilimleri Enstitüsü Dergisi, 25(2),* 208–216.

[27] Hayatoğlu, F. (2021). *Probiyotik Bakteri İlavesi ile Üretilen Ayranların Fiziksel, Kimyasal ve Mikrobiyolojik Özellikleri* (Master's Dissertation, Afyon Kocatepe University).

[28] Akçay, F. (2016). *Acılı Ayran Üretimi ve Bazı Özelliklerinin Araştırılması* (Master's Dissertation, Ondokuz Mayıs University).

[29] Temen, Y. (2018). Ayran With Quinoa Flour and Its Properties (Master's Dissertation, Council of Higher Education and Theses Database).

[30] Ürkek, B., Gürmeriç, H. E., & Şengül, M. (2021). Chia (Salvia Hispanica L.) İlavesinin Dondurmanın Fizikokimyasal ve Duyusal Özelliklerine Etkisi. *Gıda, 46(1),* 180–189.

**International Journal of Innovative Engineering Applications**

# COMPRESSION METHODS FOR SATELLITE IMAGES USING WAVELET TRANSFORM AND PERFORMANCE EVALUATION

*İbrahim Öz*[*1] iD

[1]*Ankara Yildirim Beyazit University, Technology Transfer Office, Ankara/ Turkey*

## Abstract

Research on image compression spans various fields, focusing on achieving efficient compression while preserving a specific image quality. Satellite images captured by observation satellites possess unique characteristics distinct from other images. Analyzing these specific qualities is decisive, leading to the proposal of tailored compression methods and transforms suitable for satellite image characteristics. This study comprehensively assesses the performance of six well-known compression methods in the literature, utilizing wavelet transform and metrics such as bits per pixel (BPP), compression ratio (CR), Peak Signal-to-Noise Ratio (PSNR), calculation time (CT), and Mean Squared Error (MSE). The compressed satellite images, generated through six methods and the Coif3 wavelet, are systematically compared and evaluated using performance metrics. The average values obtained for all six methods are 96.37%, 47.10 dB, and 7.92 seconds for CR, PSNR, and CT receptively, while WDR exhibits CR at 96.36%, PSNR at 48.84 dB, and CT at 6.58 seconds. The findings indicate that the Wavelet Difference Reduction (WDR) compression method utilizing the Coif3 wavelet outperforms others when considering all parameters together. We suggest that operators and manufacturers choose wavelet transform and WDR compression methods for effective compression of observation satellite images to achieve optimal results.

# DALGACIK DÖNÜŞÜMÜ İLE UYDU GÖRÜNTÜSÜ SIKIŞTIRMA METOTLARI VE PERFORMANS DEĞERLENDİRMESİ

## *Özet*

Görüntü sıkıştırma üzerine birçok alanda araştırma yapılmakta ve hedef belirli bir görüntü kalitesini korurken iyi bir sıkıştırma oranı elde etmektir. Gözlem uyduları tarafından çekilen uydu görüntüleri, diğer görüntülerden farklı özelliklere sahiptir. Bu özelliklerin analizi ile bu alana özgü dönüşüm ve sıkıştırma teknikleri geliştirilebilir. Bu çalışmada uydu görüntüsü sıkıştırılmış, dalgacık dönüşümü ve literatürde çok bilinen altı sıkıştırma yönteminin performansı; piksel başına bit (PBB), sıkıştırma oranı (SO), tepe sinyal gürültü oranı (TSGO), hesaplama süresi (HS) ve ortalama kare hata (OKH) gibi ölçütler kullanarak kapsamlı bir şekilde değerlendirilmiştir. Coif3 dalgacık dönüşümü ve bu altı sıkıştırma metodu kullanılarak elde edilen sıkıştırılmış uydu görüntüsü sistematik olarak karşılaştırılırmış ve değerlendirilmiştir. Altı yöntemin ortalama değerleri SO için %96.37, TSGO için %47.10 db ve HS için7.92 saniye iken, WDR metodunda SO, %96.36, TSGO %48.34 db ve HS 6.58 saniye olarak elde edilmiştir. Bulgular, Coif3 dalgacık dönüşümü kullanan WDR sıkıştırma yönteminin, tüm performans parametreleri dikkate alındığında diğer yöntemleri geride bıraktığını göstermektedir. Bu çalışma sonuçlarına göre uydu operatörleri ve işletmecilerine gözlem uydusu görüntüsü sıkıştırma işleminde başarılı sonuçlarından dolayıdalgacık dönüşümü ve WDR metodunu öneriyoruz.

## 1 Introduction

Image compression is decisive in digital data processing and transmission, especially in scientific and technological fields. The need for image compression arises from various factors, including limitations in data storage, the demand for efficient transmission, and the need to optimize available resources. [1]. Scientifically, the utilization of image compression arises from several essential considerations. Firstly, the inherent challenge of limited storage capacity confronts scientific datasets, particularly those generated by sources like remote sensing satellites [2-5] or medical imaging devices. This results in the need to condense data without compromising crucial

*Corresponding author.

E-mail address: ibrahimoz@gazi.edu.tr (İ. Öz)

information [6, 7]. Moreover, bandwidth constraints pose challenges when transmitting large image files over networks with limited capacity, making compression essential for efficient data transmission. Resource optimization is another crucial aspect, as the computational and hardware resources necessary for processing extensive image data can be substantial, and compression aids in minimizing these demands. Compressed images facilitate swift data transfer and analysis in applications demanding real-time processing, such as medical diagnostics or satellite communication.

Additionally, image compression contributes to cost efficiency by mitigating expenses related to storage infrastructure and network resources. The preservation of information is a paramount concern during compression, with practical methods striving to retain critical scientific details and features within the compressed images. Lastly, in scientific endeavors like space exploration or environmental monitoring, where data is remotely collected, compression becomes indispensable for extracting relevant information while minimizing the impractical transmission of vast amounts of data back to Earth [8, 9].

Satellite imagery obtained through remote sensing technologies exhibits advancements in spatial, temporal, and spectral resolutions and increased data rates, as outlined in Table 1. This progression, however, results in escalating compression requirements due to the burgeoning wealth of information. Managing vast data volumes at each stage of the image acquisition process becomes a challenge, necessitating the application of compression techniques to streamline satellite image data [10 -12].

**Table 1.** Earth Observation Satellites and Technical Properties.

| Satellites | Swath (km) | Spatial Resolution (m) | Data rate (Mbps) |
|---|---|---|---|
| Rasat | 30 | 7.5/15 | 25 |
| Gokturk 2 | 20 | 2.5/5 | 100 |
| Göktürk 1 | 15 | 0.5/1 | 465 |
| İmece | 19 | 1/4 | 320 |
| Spot 5 | 60 | 2.5 | 128 |
| Quick Bird | 18 | 2.6 | 320 |
| Ikonos | 11 | 3.2 | 320 |

The computational load posed by large multispectral imageries and concerns about data storage and transmission underscores the urgency of employing compression methods. While lossless compression ensures data volume reduction without information loss, it becomes indispensable given the significant expense and subsequent utilization of multispectral data for extensive analysis and processing operations, including classification and target detection. In scenarios where higher compression is acceptable, lossy image compression methods can be employed to balance data reduction and preserving essential information [13-15].

Satellite images, renowned for accurately mapping geospatial features, incur challenges such as high storage requirements, hardware throughput constraints, and the need for data transmission under limited bandwidth and time windows. These limitations necessitate the utilization of image compression algorithms to alleviate dependency on constraints. Various techniques have been explored, ranging from the Direct Cosine Transform (DCT) to more computationally efficient methods like the Bandelets transform [16].

Earth Observation (EO) satellites primarily utilize onboard multispectral imagers to acquire images, employing separate sensors for different wavelengths. Multispectral images, crucial in remote sensing applications, face challenges due to the limited capabilities of onboard satellite hardware. Image compression becomes imperative to reduce onboard data storage and transmission bandwidth requirements, especially during the satellite's limited passes over ground stations. Increasing the compression ratio emerges as a primary goal to optimize resource utilization while preserving scientific information during image reconstruction on Earth [11, 17,18].

Recent studies in satellite image compression methods and performance evaluation highlight the ongoing advancements in the field. For instance, the Lightweight Bit-Depth Recovery Network for Gaofen Satellite Multispectral Image Compression [19] explores efficient recovery techniques for multispectral images, addressing the challenges of bit-depth reduction. The study Satellite Image Compression and Denoising with Neural Networks [3] leverages neural network architectures to simultaneously compress and denoise satellite imagery, demonstrating the potential of AI-driven approaches. The research on a Computationally Efficient Compression Scheme for Satellite Images [16] focuses on optimizing computational resources while maintaining image quality, catering to the constraints of onboard processing. Additionally, the study titled Efficient Onboard Compression for Arbitrary-Shaped Cloud-Covered Remote Sensing Images via Adaptive Filling and Controllable Quantization [20] introduces innovative techniques for handling complex image geometries, including cloud-covered areas, through adaptive filling and precise quantization strategies. These recent works emphasize the evolving nature of satellite image compression, aiming to improve efficiency, quality, and applicability in various remote sensing scenarios.

The spectrum of image compression schemes falls into two main categories: lossless and lossy. While lossless compression, exemplified by the CCSDS 123 algorithm, maintains information integrity, lossy compression, such as JPEG2000, accepts a controlled amount of data loss for significantly higher compression ratios. In this context, DWT-based compression techniques gain prominence over DCT-based methods, offering multi-resolution transforms and achieving superior compression ratios with enhanced reconstructed image quality [13, 22-24].

Notably, some satellite missions, including Mars Exploration Rover, Rasat, X-Sat, and Pleiades-HR, demonstrate the prevalence of wavelet-based compression techniques in handling payloads. This underscores the applicability of such methods in the developing landscape of satellite technology.

## 2 Wavelet Transform and Compression Methods

The wavelet transform is a versatile tool with applications in diverse fields, including fault detection, medical applications, and crop recognition [23, 27- 30]. Its relevance continues to grow, making it an emerging field of study.

Wavelet-based image compression is a process where individual images are transformed and analyzed. The wavelet transform breaks down an image into its frequency components, creating a multi-resolution representation. This transformation is effective for compression as it eliminates unnecessary or less noticeable image data while keeping important visual information intact. The process involves several steps, starting with the application of wavelet transforms and progressing through quantization and, coding i.e., Progressive Coefficients Significance Methods (PCSM), ultimately resulting in the creation of a compressed image, as depicted in Figure 1.



**Figure 1.** Basics steps of image compression: Transform, Quantization, and Coding (PCMS).

The first step involves the transformation of the image, where it undergoes decomposition into wavelet coefficients. This process is typically executed using techniques like the discrete wavelet transform (DWT) or the lifting scheme. Composing the image in this manner enables extracting key features and details.

Following the transformation, the next step is quantization. During this stage, the coefficients obtained from the wavelet transformation are quantized. Higher frequency and less perceptually significant coefficients are subjected to more aggressive quantization. This step is crucial in prioritizing and preserving essential image information while efficiently managing data size.

The final step in wavelet-based image compression is entropy coding. This involves the application of coding techniques such as Huffman coding or arithmetic coding. The primary objective here is to compress the quantized coefficients further, optimizing the storage and transmission of the compressed image [31, 32].

Collectively, these steps form a systematic approach to wavelet-based image compression, demonstrating its effectiveness in various applications. This process reduces data size and ensures the retention of critical image details, making it a valuable technique in fields requiring efficient data management and transmission.

In the specific domain of wavelet-based image compression, a series of sequential steps are employed to achieve efficient data reduction. Satellite image compression is essential for optimizing storage and transmission bandwidth without compromising crucial information,

### 2.1 Overview of Coif3 Wavelet

The Coif3 wavelet, short for Coiflet-3, belongs to the Coiflets family, a class of wavelets designed to balance smoothness and vanishing moments. The Coif3 wavelet, in particular, possesses three vanishing moments, providing effective localization in both time and frequency domains. The scaling function, responsible for generating a Coiflet, is formulated as the solution to the scaling equation [29, 30].

$$\psi(x) = \sum_{k=2-N}^{1} (-1)^k a_{1-k} \phi(2x - k) \qquad (1)$$

where the $\phi$ scaling coefficients are selected to ensure that the associated scaling functions and wavelets have the necessary properties.

The Coif3 wavelet's three vanishing moments ensure that the wavelet function cancels out polynomials of degree two. This property aids in capturing and representing details in the signal effectively [32].

$$\phi(x) = 2 \sum_{k \epsilon Z} h_k \phi(2x - k) \qquad (2)$$

The scaling coefficients $h_k$ are determined to ensure that the corresponding scaling functions and wavelets possess the necessary properties.

Figure 2 represents Coif3 wavelet functions. Coif3 wavelet is orthogonal, forming a complete and orthonormal basis for representing signals. Orthogonality simplifies computations and ensures energy preservation during the transformation process.

Coif3 wavelet balances regularity and smoothness, making it well-suited for applications where preservation of fine details is crucial, such as in image compression.

The Coif3 wavelet's characteristics contribute to an effective and balanced decomposition, ensuring that both high and low-frequency details are appropriately represented.
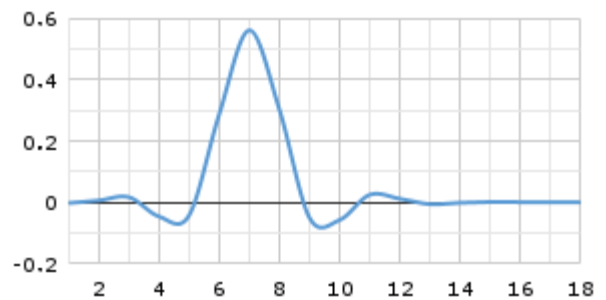


**Figure 2.** Coif3 wave function.

We chose the Coif3 wavelet based on the outcomes of the PhD dissertation titled 'Image and Video Compression Using Two-Dimensional Wavelet Transform' [24]. In our study, we implemented the Coif3 wavelet with a 4-level decomposition in our compression methods. Opting for higher decomposition levels enhances image quality. To strike a balance and address concerns like computation time, we specifically chose a 4-level decomposition for our research. This process involves breaking the image into wavelet coefficients, representing various frequency components. Following the approach outlined in the mentioned thesis, for Huffman coding with a compression ratio of 10 applied to a standard house image, the PSNR values are 35.10, 36.71, 36.94, and 39.99 dB for

decomposition levels 1, 2, 3, and 4, respectively. Notably, all methods in our study incorporate the Coif3 wavelet transform during the compression process. This decision is made to balance computational efficiency and the ability to capture details present in the image [24].

Figure 3 presents a detailed representation of a four-level decomposition of the test satellite images. Using the Coif3 wavelet, this process carefully breaks down the image into different components, capturing the overall structure and finer details. The result includes approximation and detailed coefficients covering horizontal, diagonal, and vertical components. This multi-level decomposition is essential for gaining insights into the intrinsic characteristics of satellite imagery.
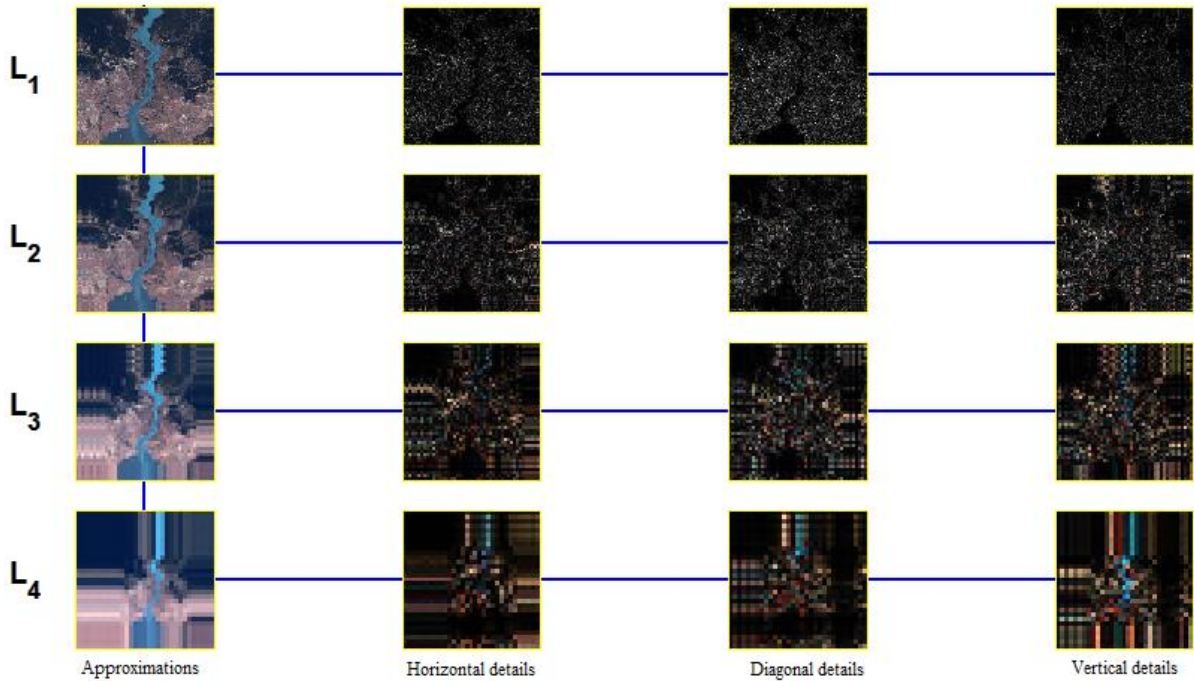


**Figure 3.** Four-level image decomposition and approximations, horizontal details, diagonal details and vertical details for each level.

The acquired coefficients undergo a crucial phase in the analytical process in the next step. Six distinct compression methods are systematically applied to these coefficients, aiming to evaluate and compare the efficiency of each method. This meticulous analysis delves into how well these compression techniques handle the diverse and intricate information embedded within the coefficients. By scrutinizing the compressed results, we gain valuable insights into the methods' ability to reduce data without sacrificing the essential features and nuances in the satellite images. The intricate dance between Coif3 wavelet decomposition and subsequent compression methods unfolds, shedding light on optimizing storage and transmission while preserving the scientific significance of satellite imagery.

### 2.2 Methods to Compress Satellite Image

This study thoroughly evaluated the effectiveness of six widely recognized Progressive Coefficients Significance Methods (PCSM), based on an extensive analysis [33]. These six methods were intentionally selected due to their broad popularity in the literature, especially in image compression and other related applications [34-36]. The raw satellite images used in this research were sourced from Rasat EO satellites, further emphasizing the relevance of these methods for satellite image compression.

### 2.2.1 Embedded Zero Tree Wavelet (EZW)

The Embedded Zero Tree Wavelet algorithm (EZW) is a valuable image compression technique that generates a fully embedded bit stream for image coding. Remarkably competitive in compression performance with known techniques, this method requires no training, pre-stored codebooks, or prior image source knowledge. EZW is rooted in four fundamental concepts: discrete wavelet transform (DWT) or hierarchical sub-band decomposition, prediction of information absence across scales, entropy-coded successive-approximation quantization, and universal lossless data compression through adaptive arithmetic coding. The algorithm's consecutive operation is noteworthy, ceasing upon meeting a target bit rate or distortion. The encoding process represents a pivotal aspect of EZW.

### 2.2.2 Set-Partitioning In Hierarchical Trees (SPIHT):

SPIHT is a fully embedded wavelet coding algorithm prioritizing information in decreasing energy levels. It allocates the bit budget between encoding the tree map and the significance information, enabling precise rate control and reasonable computational complexity. Reportedly surpassing other coding techniques like DCT and EZT, SPIHT, an enhanced version of EZW, has demonstrated superior performance with high PSNR values for diverse images. Its widespread adoption makes it a standard for

comparing subsequent wavelet-based image compression algorithms.

### 2.2.3 Spatial-Orientation Tree Wavelet (STW)

STW is essentially an adaptation of the SPIHT algorithm, differing only in the organization of coding output. It utilizes a state transition model to encode zero tree information, deviating from EZW's approach. The 3D_spiht scheme, an extension from 2D SPIHT, maintains partial ordering by magnitude, ordered bit-plane transmission, and the SPIHT algorithm's principles.

### 2.2.4 Wavelet Difference Reduction (WDR)

The WDR algorithm is a straightforward procedure involving a wavelet transform applied to the image, followed by bit-plane-based WDR encoding for the wavelet coefficients.

### 2.2.5 Adaptively Scanned Wavelet Difference Reduction (ASWDR)

ASWDR is a generalization of the WDR method by Tian and Wells, producing an embedded bit stream for progressive transmission and encoding precise indices for significant transform values. This capability facilitates Region of Interest (ROI) and various image processing operations on compressed image files [12].

### 2.2.6 SPIHT_3D

SPIHT_3D exploits self-similarity across spatial-temporal orientation trees, providing a wholly-embedded compressed bit stream. This characteristic allows for progressive video quality, enabling the algorithm to stop at any compressed file size or run until nearly lossless reconstruction. Such flexibility is desirable in applications like high-definition television.

### 2.3 Evaluation Metrics

In this study, we employ the following evaluation metrics to assess the performance of the compression methods applied to satellite images [33, 34].

### 2.3.1. Bit Per Pixel (bpp)

Bpp is a fundamental metric representing the average number of bits required to encode each pixel in the compressed image. It provides insights into the overall efficiency of the compression methods regarding data representation.

$$bpp = \frac{n*8}{H*W} \qquad (4)$$

where H: the height of an image, W: the width of an image.

### 2.3.2. Compression Ratio

The compression ratio measures the extent to which the image size is reduced after compression. It is calculated as the ratio of the original image size to the compressed image size.

$$CR = \left(1 - \frac{h_c}{h_i}\right) * 100 \qquad (5)$$

where, $h_c$: the number of bits in the compressed image, $h_i$: the number of bits in the original image.

### 2.3.3. Mean Squared Error (MSE)

MSE represents the average squared difference between the original and compressed images. Lower MSE values indicate better fidelity in image reconstruction.

$$MSE = \frac{1}{mn}\sum_{i=0}^{m=1}\sum_{j=0}^{n=1}|X(i,j) - X_c(i.j)|^2 \qquad (6)$$

where M and N represent the image's size, X represents the given input image and $X_c$ represents the reconstructed image.

### 2.3.3. Peak Signal-to-Noise Ratio (PSNR)

PSNR quantifies the quality of the compressed image by comparing it to the original. Higher PSNR values indicate better preservation of image quality.

$$PSNR = 10log_{10}\left(\frac{max^2}{MSE}\right) \qquad (7)$$

where max : the maximum possible pixel value of the image.

### 2.3.5. Calculation Time

The time taken by each compression method for processing is a critical factor, especially in real-time applications. It provides insights into the computational efficiency of the methods.

$$CT = cpu_{t2} - cpu_{t1} \qquad (8)$$

where $cpu_{t2}$: process stop time, $cpu_{t1}$: process start time.

A satellite test image showcasing diverse characteristics served as the focal point for our analysis. Employing the Coif3 wavelet during the transform phase, we applied six compression methods to compress the image. Subsequently, the resultant images underwent evaluation using predefined metrics.

Systematic comparisons were made among the outcomes of each compression method, relying on evaluation metrics such as bits per pixel (bpp), compression ratio, Peak signal-to-noise ratio (PSNR), Mean Squared Error (MSE), and calculation time. This comprehensive assessment provided insights into the performance of each method across these criteria.

The results derived from the satellite images were compared with those obtained from a standard test image commonly employed in compression studies to verify our findings. This comparative analysis further validated the effectiveness and reliability of our compression methods in handling satellite image data.

## 3    Results and Discussion

In this study, we carefully compressed a satellite test image using six distinct compression methods. We specifically chose the Coif3 wavelet for the transformation phase due to its exceptional performance, seamlessly meeting the study's requirements. The decision to use Coif3 is rooted in its proven effectiveness in balancing detail capture and computational efficiency. The assessment is conducted based on key statistical parameters such as bits per pixel (BPP), compression ratio (CR), Peak signal-to-noise ratio (PSNR), calculation time, and Mean Squared Error (MSE).

Figure 4 presents the results of satellite image compression using six analyzed compression methods, considering different numbers of encoding loops. It is important to note that the Coif3 wavelet transformer remains constant across all scenarios. Figure 4a illustrates the compression methods bit-per-pixel (bpp) performances. Notably, the WDR method achieves the best values, and the SP-3D method exhibits the lowest curve. Figure 4b provides insights into the calculation time, with the SPIHT method demonstrating the most efficient performance among the methods.

In contrast, the EZW method lags behind with the least favorable results. Figures 4c and 4d depict the peak signal-to-noise ratio (PSNR) and compression ratio (CR) performances, respectively. The WDR method yields higher PSNR, while three other methods demonstrate comparable results. Regarding compression ratio, the WDR method excels, offering the most efficient compression, whereas the SP-3D method exhibits the least favorable results.
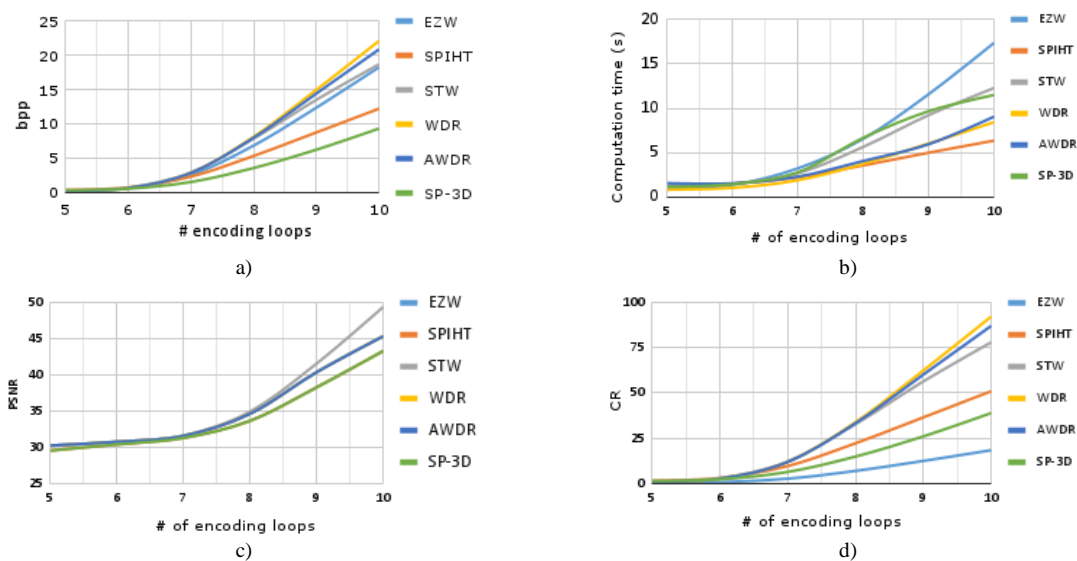


**Figure 4.** Satellite image compression performances using six methods from 5 to 10 encoding loops a) bit per pixel b) calculations time c) image quality, PSNR d) compression ratio.

Within Figure 5, a visual narrative unfolds, presenting a triptych of images that encapsulate the transformative journey of a test satellite image. The pristine satellite image on the left stands as the original, untouched representation. In the center, we witness the intricate web of details unveiled through the original decomposition process, showcasing the distinct components obtained through the Coif3 wavelet family. Finally, on the right emerges the reconstructed image, a harmonious synthesis achieved through the marriage of Coif3 wavelet decomposition and the WDR compression method, meticulously executed across 10 encoding loops.

In this scenario, utilizing the Coif3 wavelet family and the WDR compression method reveals a result adorned with a remarkable 45 dB PSNR (Peak Signal-to-Noise Ratio) value. This metric, indicative of the fidelity between the original and reconstructed images, underscores the method's proficiency in retaining crucial information during the compression process. Furthermore, the Compression Ratio (CR) of 8% highlights the adeptness of the chosen compression strategy in significantly reducing data size while maintaining a balance that allows for efficient storage and transmission.
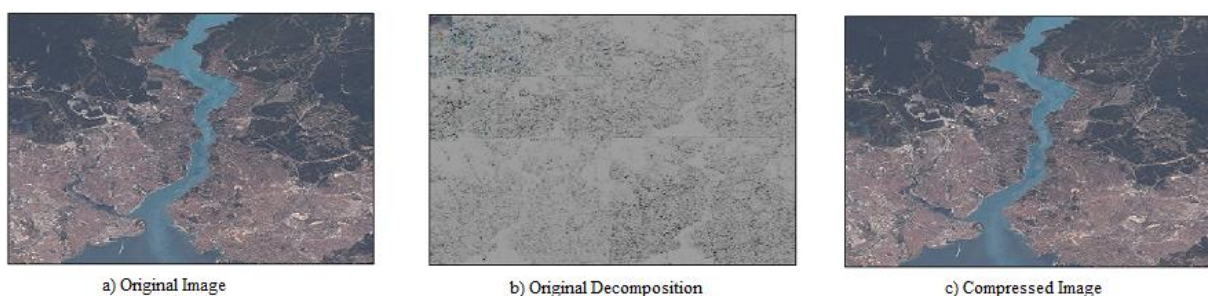


**Figure 5.** a) Original satellite image b) four-level wavelet decomposition c) reconstructed image.

These visual and quantitative insights provide a captivating glimpse into the transformative capabilities of the Coif3 wavelet family and the WDR compression method, showcasing their collaborative prowess in striking a harmonious balance between preservation and efficiency in the realm of satellite image processing.

Table 2 presents the statistical results of satellite image compression employing various compression methods for encoding loops ranging from 5 to 10. Notably, the WDR method attains the best bit per pixel (bbp) value at 15.62 bpp, displaying its efficiency in data representation. The highest compression ratio (CR) is achieved using the EZW method, reaching an impressive 96.55 db. In terms of peak signal-to-noise ratio (PSNR), the WDR method excels, attaining the highest value at 48.85. Similarly, the mean squared error (MSE) is optimal

for the WDR, EZW, and ASWDR methods, all obtaining the best MSE at 35.51. Furthermore, the WDR method stands out for its computational efficiency, boasting the lowest computation time at 6.58 seconds in 10 loops, emphasizing its effectiveness in achieving a balance between compression performance and computational speed.

The overall performance of compression methods can be expressed as;

$$P_{all} = CR + PSNR + (CT_{max} - CT) \qquad (9)$$

WDR demonstrates superior overall performance, achieving a value of 152.34, as illustrated in the last row of Table 2.

**Table 2.** Performance values of Satellite Image Coif3 Transform and Six Compression Methods.

|  | EZW | | SP | | STW | | WDR | | ASWDR | | SP3D | |
|---|---|---|---|---|---|---|---|---|---|---|---|---|
|  | max | Average | max | Average | max | Average | max | Average | max | Average | max | Average |
| bpp | 13.32 | 5.26 | 6.59 | 2.94 | 9.29 | 3.44 | 15.62 | 6.08 | 15.06 | 5.96 | 5.32 | 2.33 |
| CR | 96.55 | 78.07 | 95.46 | 87.76 | 97.05 | 85.69 | 96.36 | 74.68 | 96.28 | 75.19 | 96.50 | 90.29 |
| PSNR | 48.34 | 40.07 | 44.45 | 35.52 | 48.65 | 37.81 | 48.84 | 40.07 | 48.34 | 40.07 | 44.45 | 35.52 |
| CT | 13.72 | 6.40 | 5.47 | 2.90 | 7.13 | 3.49 | 6.58 | 2.85 | 7.75 | 3.50 | 6.86 | 3.67 |
| MSE | 36.51 | 12.87 | 107.64 | 35.80 | 58.92 | 21.99 | 36.51 | 12.87 | 36.51 | 12.87 | 107.64 | 35.80 |
| $P_{all}$ | 144.89 | 125.47 | 148.16 | 134.11 | 152.29 | 133.73 | 152.34 | 125.63 | 150.59 | 125.49 | 117.35 | 135.87 |

It is crucial to ensure satisfaction with the results by comparing them with established references. Therefore, for the purpose of comparative analysis, the results obtained from WDR are compared with those from the well-known Huffman coding.

Table 3 presents a comprehensive comparative analysis of compression performance for satellite images, utilizing both Huffman coding (huf_lvl) and Wavelet Difference Reduction (WDR) techniques. The satellite images undergo Coif3 wavelet decomposition at level 4, and various statistical parameters are assessed by selecting the number of encoding loops from 5 to 10 in compression methods to evaluate their effectiveness.

In the case of Huffman coding, the bits per pixel (BPP) range from a minimum of 0.66 to a maximum of 14.00, with an average of 8.35, indicating variations in data representation. Compression ratios (CR) range from 41.68 to 97.25, with an average of 65.22, significantly reducing data size. Peak Signal-to-Noise Ratio (PSNR) values vary between 31.00 and 48.74, with an average of 39.94, reflecting the quality of the compressed images. The computational efficiency is evident in the calculation time, ranging from 0.41 to 3.28 seconds, with an average of 1.85 seconds. Mean Squared Error (MSE) values range from 0.87 to 51.71, averaging 14.73, representing the deviation between the original and compressed images.

On the other hand, Wavelet Difference Reduction (WDR) outperforms in bits per pixel (BPP), with a range of 0.87 to 15.62 and an average of 6.08, displaying its efficiency in data representation. Compression ratios (CR) for WDR vary between 34.93 and 96.36, with an average of 74.68, indicating a substantial reduction in data size. PSNR values for WDR range from 32.51 to 48.34,

averaging at 40.07, highlighting the method's proficiency in preserving image quality. WDR also demonstrates computational efficiency, with calculation times ranging from 1.08 to 6.58 seconds and an average of 2.85 seconds. MSE values for WDR span from 0.95 to 36.51, averaging 12.87, emphasizing the accuracy of the compressed images.

In terms of overall performance, the Huffman coding method scores 149.29, while the WDR technique achieves a slightly lower value of 144.70. These values are indicative of the effectiveness of the respective compression methods when considering multiple performance metrics

This comprehensive comparison offers nuanced insights into the performance of Huffman coding and Wavelet Difference Reduction. It provides a detailed understanding of their strengths and limitations across key statistical parameters in satellite image compression.

**Table 3** Performance Comparison of Satellite Image with Coif3 Transform and Decomposition Level-4: Huffman vs. WDR.

|  | Huffman | | | WDR | | |
|---|---|---|---|---|---|---|
|  | max | min | avg | max | min | Average |
| bpp | 14.00 | 0.66 | 8.35 | 15.62 | 0.87 | 6.08 |
| CR | 97.25 | 41.68 | 65.22 | 96.36 | 34.93 | 74.68 |
| PSNR | 48.74 | 31.00 | 39.94 | 48.84 | 32.51 | 40.07 |
| CT | 3.28 | 0.41 | 1.85 | 6.58 | 1.08 | 2.85 |
| MSE | 51.71 | 0.87 | 14.73 | 36.51 | 0.95 | 12.87 |
| $P_{all}$ | 149.29 | 78.85 | 109.90 | 144.70 | 72.94 | 118.49 |

A well-known daily house image was selected for evaluation to assess the performance of Wavelet Difference Reduction (WDR) in satellite image compression. Both images were compressed by employing WDR and Huffman methods while maintaining the Coif3 wavelet transform.

Table 4 comprehensively compares compression performances for daily house images using Huffman coding and Wavelet Difference Reduction (WDR) techniques. The house images undergo Coif3 wavelet decomposition at level 4, and various statistical parameters are evaluated to assess the efficiency of the compression methods.

For Huffman coding, the bits per pixel (BPP) values range from a minimum of 1.34 to a maximum of 11.66, with an average of 6.87, illustrating variations in data representation. Compression ratios (CR) range from 51.43 to 94.43, with an average of 71.39, indicating a substantial reduction in data size. Peak Signal-to-Noise Ratio (PSNR) values vary between 36.42 and 54.67, with an average of 47.02, reflecting the quality of the compressed images. The computational efficiency is evident in the calculation time, ranging from 0.50 to 3.11 seconds, with an average of 1.88 seconds. Mean Squared Error (MSE) values range from 0.22 to 14.84, with an average of 3.07, representing the deviation between the original and compressed images.

On the other hand, Wavelet Difference Reduction (WDR) outperforms in bits per pixel (BPP), with a range of 0.35 to 9.86 and an average of 3.40, displaying its efficiency in data representation. Compression ratios (CR100) for WDR vary between 58.92 and 98.54, with an average of 85.85, indicating a substantial reduction in data size. PSNR values for WDR range from 31.22 to 45.00, averaging at 37.19, highlighting the method's proficiency in preserving image quality. WDR also demonstrates computational efficiency, with calculation times ranging from 0.84 to 3.22 seconds and an average of 1.56 seconds. MSE values for WDR span from 2.05 to 49.05, averaging at 20.22, emphasizing the accuracy of the compressed images.

**Table 4** Performance Comparison of House Image with Coif3 Transform and Decomposition Level-4: Huffman vs. WDR.

|  | Huffman | | | WDR | | |
|---|---|---|---|---|---|---|
|  | max | min | avg | max | min | Average |
| bpp | 11.66 | 1.34 | 6.87 | 9.86 | 0.35 | 3.40 |
| CR | 94.43 | 51.43 | 71.39 | 98.54 | 58.92 | 85.85 |
| PSNR | 54.67 | 36.42 | 47.02 | 45.00 | 31.22 | 37.19 |
| CT | 3.11 | 0.50 | 1.88 | 3.22 | 0.84 | 1.56 |
| MSE | 14.84 | 0.22 | 3.07 | 49.05 | 2.05 | 20.22 |
| $P_{all}$ | 152.54 | 93.90 | 123.08 | 146.87 | 95.85 | 128.03 |

Considering the overall performances of all compression methods, the Huffman coding method exhibits a commendable score of 152.54, highlighting its effectiveness in various aspects. On the other hand, the Wavelet Difference Reduction (WDR) method performs admirably with a slightly lower yet competitive score of 146.87. These values reflect the comprehensive assessment of both techniques across multiple

performance metrics, demonstrating their respective strengths and capabilities in the context of image compression

The analysis of compression performance for both daily house and satellite images using Huffman coding and Wavelet Difference Reduction (WDR) techniques, as depicted in Tables 3 and Table 4, provides valuable insights into the effectiveness of these methods.

The Coif3 wavelet, known for combining smoothness and vanishing moments, is a valuable tool for transforming the satellite test image, capturing both spatial and spectral features. This intentional choice aims to enhance the efficiency and quality of the compression process, aligning with a systematic and informed approach. The study seeks to leverage the strengths of Coif3 to derive optimal insights and results from the compression methods employed.

The comparative analysis highlights the nuanced performance characteristics of Huffman coding and WDR when dealing with distinct image datasets. While Huffman coding demonstrates computational efficiency and competitive CR values, WDR excels in achieving lower BPP values, superior accuracy (reflected in lower MSE values), and competitive CR values. The selection between these methods would depend on the specific requirements and priorities of the given application, balancing considerations of data size reduction, computational efficiency, and image quality preservation.

## 4 Conclusion

This study evaluated the performance of six widely recognized compression methods specifically designed for satellite images. It acknowledged the unique characteristics of satellite imagery, which differ from other types of images, such as medical or everyday photos, each requiring distinct measurement metrics. The research aimed to demonstrate the impact of compression methods on satellite images while consistently utilizing the Coif3 wavelet as the transform. Key statistical parameters, including BPP, CR, PSNR, CT, and MSE, were analyzed to gain a comprehensive understanding of the strengths and limitations of each method.

WDR demonstrates superior accuracy in image reconstruction when considering all parameters together. The validation using the well-known Huffman coding further confirms the efficacy of the proposed WDR method.

Future endeavors in this research domain could focus on several promising directions. Firstly, exploring hybrid compression approaches that combine the strengths of Huffman coding and WDR could potentially yield enhanced results. Investigating the impact of varying wavelet families and decomposition levels on compression outcomes may provide valuable insights into optimizing the process further. Additionally, incorporating machine-learning techniques for adaptive compression based on image content and context could be an avenue for future exploration.

Further research efforts may also address the development of real-time compression algorithms for dynamic image data and explore the application of these compression methods in various domains, such as medical

imaging or video compression. Assessing the robustness of the compression methods under different image characteristics and exploring their performance on large-scale datasets could contribute to a more comprehensive understanding of their applicability.

In summary, the findings from this study lay the groundwork for future investigations that aim to refine existing compression methodologies, explore hybrid approaches, and adapt compression techniques to diverse and dynamic imaging scenarios. As technology advances and the demand for efficient image processing grows, continuous exploration and refinement of compression methods remain imperative for addressing evolving requirements in various scientific and technological domains.

## Declaration

Ethics committee approval is not required.

## References

[1] Othman, G., & Zeebaree, D. Q. (2020). The Applications of Discrete Wavelet Transform in Image processing: A review. *Journal of soft computing and data mining,* 1(2), 31-43.

[2] Indradjad, A., Nasution, A. S., Gunawan, H., & Widipaminto, A. (2019). A comparison of Satellite Image Compression methods in the Wavelet Domain. *In IOP Conference Series: Earth and Environmental Science* (Vol. 280, No. 1, p. 012031). IOP Publishing.

[3] De Oliveira, V. A., Chabert, M., Oberlin, T., Poulliat, C., Bruno, M., Latry, C., ... & Camarero, R. (2022). Satellite Image Compression and Denoising with Neural Networks. *IEEE Geoscience and Remote Sensing Letters*, 19, 1-5.

[4] Delaunay, X., Chabert, M., Charvillat, V., & Morin, G. (2010). Satellite Image Compression by Post-Transforms in the Wavelet Domain. *Signal processing*, 90(2), 599-610.

[5] Teke, M. (2016). Satellite Image Processing Workflow for RASAT and Göktürk-2. *Journal of Aeronautics and Space Technologies, 9*(1), 1-13.

[6] Taş, İ. Ç. Application of Panoramic Dental X-Ray Images Denoising. International *Journal of Innovative Engineering Applications*, 7(1), 13-20.

[7] Toraman, S., & Turkoglu, I. (2020). Using Wavelet Transform and Machine Learning Techniques, a Wew Method for Classifying Colon Cancer Patients and Healthy People from FTIR Signals. *Journal of the Faculty of Engineering and Architecture of Gazi University*, 35(2), 933-942.

[8] Vura, S., Patil, P., & Patil, S. B. (2023). A Study of Different Compression Algorithms for Multispectral Images. Materials Today: *Proceedings, 80,* 2193-2197.

[9] Kitaeff, V. V., Cannon, A., Wicenec, A., & Taubman, D. (2015). Astronomical Imagery: Considerations for a Contemporary Approach with JPEG2000. *Astronomy and Computing, 12*, 229-239.

[10] Ma, X. (2023). High-resolution Image Compression Algorithms in Remote Sensing Imaging. *Displays,* 102462.

[11] Yu, G., Vladimirova, T., & Sweeting, M. N. (2009). Image Compression Systems on Board Satellites. *Acta Astronautica, 64*(9-10), 988-1005.

[12] Liao, L., Xiao, J., Li, Y., Wang, M., & Hu, R. (2020). Learned Representation of Satellite Image Series for Data Compression. Remote Sensing, 12(3), 497.

[13] Shihab, H. S., Shafie, S., Ramli, A. R., & Ahmad, F. (2017). Enhancement of Satellite Image Compression Using a Hybrid (DWT–DCT) Algorithm. *Sensing and Imaging,* 18, 1-30.

[14] Swetha, V., Patil, G. P., & Patil, B. S. (2021, July). Lossless Compression of Satellite Images using a Versatile Hybrid Algorithm. *In IOP Conference Series: Materials Science and Engineering* (Vol. 1166, No. 1, p. 012048). IOP Publishing.

[15] Bacchus, P., Fraisse, R., Roumy, A., & Guillemot, C. (2022, July). Quasi Lossless Satellite Image Compression. In IGARSS 2022-2022 *IEEE International Geoscience and Remote Sensing Symposium* (pp. 1532-1535). IEEE.

[16] Jamuna Rani, M., & Azhagu Jaisudhan Pazhani, A. (2022). Computational Efficient Compression Scheme for Satellite Images. *Earth Science Informatics, 15*(3), 1723-1736.

[17] Faria, L. N., Fonseca, L. M., & Costa, M. H. (2012). Performance Evaluation of Data Compression Systems Applied to Satellite Imagery. *Journal of Electrical and Computer Engineering,* 2012, 18-18.

[18] Hagag, A., Hassan, E. S., Amin, M., Abd El-Samie, F. E., & Fan, X. (2017). Satellite Multispectral Image Compression Based on Removing Sub-bands. *Optik,* 131, 1023-1035.

[19] Zhang, W., Li, D., Zhang, H., Yu, P., & Gao, W. (2024). Lightweight Bit-Depth Recovery Network for Gaofen Satellite Multispectral Image Compression. *IEEE Journal of Selected Topics in Applied Earth Observations and Remote Sensing*.

[20] Wang, K., Jia, J., Zhou, P., Ma, H., Yang, L., Liu, K., & Li, Y. (2024). Efficient Onboard Compression for Arbitrary-Shaped Cloud-Covered Remote Sensing Images via Adaptive Filling and Controllable Quantization. *Remote Sensing,* 16(18).

[21] Yilmaz, Ö., Aksoy, M., Kesilmiş, Z. (2019). Misalignment Fault Detection by Wavelet Analysis of Vibration Signals. *International Advanced Researches and Engineering Journal, 3*(3), 156-163.

[22] Oz, I., Oz, C., Yumusak, N. (2001) Image Compression Using 2-D Multiple-Level Discrete Wavelet Transform (DWT). *Eleco 2001 International Conference on Electrical and Electronics Engineering,* Turkey

[23] Akmaz, D. (2022). Recognition Of Power Quality Events Using Wavelet Transform, K-Nearest Neighbor Algorithm And Gain Ratio Feature Selection Method. *International Journal of Innovative Engineering Applications, 6*(1), 42-47.

[24] Oz, I.(2006). *Image and Video Compression by Using Two Dimensional Wavelet Transform* (Doctoral dissertation, Sakarya University).

[25] Saken, M., Yağci, M. B., & Yumuşak, N. (2021). Impact of Image Segmentation Techniques on Celiac Disease Classification Usingscale Invariant Texture Descriptors for Standard Flexible Endoscopic Systems. *Turkish Journal of Electrical Engineering and Computer Sciences*, 29(2), 598-615.

[26] Coşkun, M., Gürüler, H., Istanbullu, A., Peker, M. (2015). Determining the Appropriate Amount of Anesthetic Gas Using DWT and EMD Combined with Neural Network. *Journal of medical systems,* 39, 1-10.

[27] Coşkun, M., & İstanbullu, A. (2012). EEG İşaretlerinin FFT ve Dalgacık Dönüşümü ile Analizi. XIV. *Akademik Bilişim Konferansı*, Uşak, Türkiye.

[28] Akay, M., & Tuncer, T. (2021). Çok Seviyeli Dalgacık Dönüşümü ve Yerel İkili Örüntüler Tabanlı Otomatik EEG Duygu Tanıma Yöntemi. *International Journal of Innovative Engineering Applications,* 5(2), 75-80.

[29] Şengür, A., Türkoğlu, İ., & Ince, M. C. (2006). A Comparative Study on Entropic Thresholding Methods. *IU-Journal of Electrical & Electronics Engineering, 6*(2), 183-188.

[30] Yumusak, N., Temurtas, F., Cerezci, O., & Pazar, S. (1998, August). Image thresholding using measures of fuzziness. In IECON'98. *Proceedings of the 24th Annual Conference of the IEEE Industrial Electronics Society* (Cat. No. 98CH36200) (Vol. 3, pp. 1300-1305). IEEE.

[31] Černá, D., Finěk, V., & Najzar, K. (2008). On the exact values of coefficients of coiflets. *Open Mathematics, 6*(1), 159-169.

[32] Taher, M. M., & Redha, S. M. (2022). Use The Coiflets and Daubechies Wavelet Transform To Reduce Data Noise For a Simple Experiment. *Iraqi Journal of Statistical Sciences, 19*(2), 91-103.

[33] Kumar, R., & Singh, S. (2014). Comparative Analysis of Wavelet Based Compression Methods. *International Journal of Computer Networking, Wireless and Mobile Communications,* 143-150.

[34] Oz, I. (2024). Comparative Analysis of Wavelet Families in Image Compression, Featuring the Proposed New Wavelet. *Turkish Journal of Science and Technology*, 19(1), 279-294. https://doi.org/10.55525/tjst.1428424

[35] Marangoz, A. M., Sefercik, U. G., & Damla, YÜCE, (2020). Three-dimensional earth modelling performance analysis of Gokturk-2 satellite. *Turkish Journal of Engineering, 4*(3), 164-168.

[36] Wang, K., Jia, J., Zhou, P., Ma, H., Yang, L., Liu, K., & Li, Y. (2024). Efficient Onboard Compression for Arbitrary-Shaped Cloud-Covered Remote Sensing Images via Adaptive Filling and Controllable Quantization. *Remote Sensing,* 16(18).

# INVESTIGATION OF TOOL WEAR AND THRUST FORCE IN DRILLING AISI 316 AUSTENITIC STAINLESS STEEL USING ELECTROPHORESIS METHOD

*Aybars Mahmat*[*1] iD

[1]*Munzur University, Faculty of Engineering, Departmant of Mechanical Engineering, Tunceli, Turkey*

## Abstract

Cutting tool costs are an important component of machining. For this reason, improving machining methods in machining affects the life of the cutting tool. Recently, various machining methods have been used to extend tool life by reducing cutting tool wear. One of these methods is electrophoresis-assisted processing. Electrophoresis-assisted machining is a non-traditional machining method created by the impact of abrasive nanoparticles on the machining area with the help of the generated electric field. Electrophoresis-assisted machining increases the machinability of difficult-to-machine materials with high strength and hardness properties compared to traditional machining methods. In this study, the impacts of various cutting parameters on the drilling performance of AISI 316 L stainless steel material were searched using electrophoresis-assisted drilling (EAD) and conventional drilling (CD) methods. In the study, SiC powder was used as nanoparticles in the solution obtained to create the electric field. Within the scope of the experiments, the effects of different machining methods, cutting speeds and feed rates on thrust forces and cutting tool wear values were experimentally examined. As a result of the investigations, the cutting tool wear and thrust cutting force obtained with EAD are better than CM. Increasing feed rate and cutting speed increased cutting tool wear in both machining methods. It has been determined that the thrust force decreases as the cutting speed increases, while it increases as the feed rate increases.

*Keywords: Electrophoresis, drilling, cutting force, tool wear, AISI 316.*

# AISI 316 ÖSTENİTİK PASLANMAZ ÇELİĞİN ELEKTROFOREZ YÖNTEMİYLE DELİNMESİNDE TAKIM AŞINMASI VE İTME KUVVETİNİN İNCELENMESİ

## Özet

Kesici takım maliyetleri talaşlı imalat için önemli bir bileşendir. Bu nedenle talaşlı imalatta işleme yöntemlerinin iyileştirilmesi kesici takım ömrüne etki etmektedir. Kesici takım aşınmasını azaltarak takım ömrünün uzatılması için son zamanlarda farklı işleme yöntemleri kullanılmaktadır. Bu yöntemlerden biri de elektroforez destekli işlemedir. Elektroforez destekli işleme oluşturulan elektrik alan yardımıyla aşındırıcı nano partiküllerin işleme alanına etki etmesiyle oluşturulan geleneksel olmayan işleme yöntemidir. Elektroforez destekli işleme, geleneksel işleme yöntemlerine kıyasla yüksek mukavemet ve sertlik özelliklerine sahip, işlenmesi zor malzemelerin işlenebilirliğini artırır. Bu çalışmada AISI 304 paslanmaz çelik malzemesinin elektroforez destekli delme (EDD) ve geleneksel delme (GD) yöntemleri kullanılarak farklı kesme parametrelerinin delik delme performansı üzerine etkileri araştırılmıştır. Çalışmada elektrik alanını oluşturmak elde edilen çözeltide nano partikül olarak SiC toz kullanılmıştır. Deneyler kapsamında farklı işleme yöntemleri, kesme hızları ve ilerleme hızlarının itme kuvvetleri ve kesici takım aşınma değerleri üzerindeki etkileri deneysel olarak incelenmiştir. İncelemeler sonucunda kesici takım aşınması ve itme kuvveti için en iyi sonuçlar EDD ile elde edilmiştir. Kesme hızının ve ilerleme hızının artması her iki işleme yönteminde kesici takım aşınmasını artırmıştır. İtme kuvveti kesme hızı arttıkça azalırken ilerleme hızı arttıkça arttığı tespit edilmiştir.

*Anahtar Kelimeler: Elektroforez, delme, kesme kuvveti, takım aşınması, AISI 316.*

## 1 Introduction

Cutting force and cutting tool wear are important criteria in drilling. It is difficult to control and improve these two performance characteristics with traditional machining methods. Cooling methods are an effective method on machinability. However, the rotational movement of the cutting tool removes the fluid from the cutting area and results in an increased wear of the tool although it is also dependent on the material being cut. Stainless steels are preferred in the transportation via aerospace and also in marine due to their outstanding mechanical strength and corrosion resistance. Austenitic stainless steel alloys are in the group of materials that are

difficult to cut. These steels contain high Cr and Ni. These properties make machinability difficult due to low thermal conductivity and hardening properties during machining [1], [2]. Therefore, it creates high cutting forces and cutting temperatures during machining [3]. This situation increases tool wear by increasing friction in the cutting area and causes chip accumulation on the tool tip [4], [5]. AISI 316 austenitic stainless steel is a challenging material to cut due to its distinctive machining characteristics. Its mechanical properties contribute to the difficulty of drilling this material. The workpiece undergoes hardening during the machining process, which results in increased wear on the cutting tool and a reduction in the quality of the machined surface. Furthermore, the material's inherent difficulty in undergoing deformation results in the generation of prolonged, elongated chips. These challenges have significantly constrained the utilization of AISI 316 steel, necessitating the urgent resolution of these issues within the industry. Extensive research has been conducted on the machinability of austenitic stainless steel alloys, with ongoing efforts to ascertain the optimal machining conditions. In this regard, it is crucial to investigate the most suitable machining conditions for the processing of these materials.

In machining, obtaining a quality surface, long tool life and increasing the metal removal rate are of great importance [6]. Drilling is a machining method that uses a cutting tool to remove materials from the drilling area to create a hole [7]. Tool wear, burr formation, surface quality, thrust forces and tool life are important parameters in drilling. In machining, the friction occurring in the cutting zone creates high cutting temperature and cutting pressure. Drilling becomes difficult because heat is concentrated in the cutting area [8]. Accelerated wear creates various mechanisms on the cutting tool. The various wear mechanisms depend on the cutting parameters and cooling methods in the cutting zone [9]. Tool wear influences surface quality and cutting performances [10], [11]. During the machining process, changes occur in the cutting tool geometry due to tool wear. Jawahir et al. [12] concluded in their study that the wear resistance and corrosion of the cutting tool have an effect on the surface quality. Kummel et al. [13] investigated the effect of cutting tool wear on machining quality and tool life. They found that increasing chip accumulation on the surface reduces wear and roughness. Considering the findings presented in the existing literature, the selection of appropriate additional techniques or process parameters during drilling and machining can enhance the machinability of the material. Consequently, the precision and efficiency of the machining process can be improved by employing alternative machining methods in conjunction with drilling.

The use of existing conventional machining methods in machining materials that are difficult to remove causes cutting tool wear and reduces machinability [14]. To increase the machining efficiency of austenitic stainless steel, researchers have proposed different cooling methods. In order to reduce wear in the cutting area, cutting temperature and cutting force must be reduced. For this reason, various cooling methods and cutting fluids are applied to the cutting area [15], [16]. Khan et al. [17]

studied the cutting performance of AISI 9310 under dry and MQL conditions. They found that MQL increased tool life and surface finish by reducing the cutting temperature. However, the use of cooling methods has negative effects on the environment and human health due to their harmful chemical substance content [18], [19]. These negative effects have led to the use of alternative methods in machining. Due to the problems mentioned above, studies on harmless cooling methods that will decrease wear have become inevitable. With the electrophoresis-assisted processing method, which is one of these methods, negativities can be eliminated by creating an electric field in the processing area. This method is a non-traditional process used to cut metals that are generally hard or difficult to cut, where a conventional process is not suitable. Electrophoresis is the movement of charged nanoparticles in solution within the electric field created in the shear zone. In electrophoresis-assisted machining, abrasive particles penetrate the machining area thanks to an electric field, increasing machining efficiency [20]. He et al. [21] investigated the surface roughness of AL6061 workpiece with electrophoresis-assisted ultrasonic machining. As a result of the experiments, they found that electrophoresis-assisted ultrasonic machining increased the surface quality compared to other machining methods.

In this study, the positive/negative aspects of the performance characteristics were investigated in the machining of AISI 316 L austenitic stainless steel using the electrophoresis method, which is new and rare in machining, and the best solution methods that will create an alternative to traditional machining methods were determined. In the study, tool wear and thrust force were determined as performance characteristics. By applying the EAD method, it was aimed to increase the tool life as a result of minimizing the thrust force and cutting tool wear. It was seen in the obtained results that the EAD method was not used in drilling and this method increased the machinability compared to other machining methods. According to the results obtained, this study will make serious contributions to minimizing the current problems in the machining of engineering materials with similar mechanical properties to AISI 316 L austenitic stainless steel.

## 2 Materials and Methods

### 2.1 Experimental Setup

This study was established to investigate the impacts of different machining methods and different cutting parameters on cutting tool wear and thrust force in drilling experiments of AISI 316 L austenitic stainless steel. Workpieces with dimensions of 90x45x5 mm were used in the drilling experiments. The chemical composition and physical properties of AISI 316 L austenitic stainless steel are given in Table 1.

In the electrophoresis method, the voltage (V) applied between two electrodes using a direct current (DC) source and the distance (d) between the electrodes lead to the formation of an electric field (E=V/d). To create an electric field between two electrodes, charged abrasive particles are suspended in the working fluid tank and move towards the oppositely charged electrode [22]. Direct current (DC) is

used as the electrical source. To create an electric field, the cutting tool is positively charged by being connected to the anode end, and the solution containing the working fluid is negatively charged by being connected to the cathode end. Thus, an electric field is created between the working fluid and cutting tool. Thanks to the electric field created, the nanoparticles move to the worn areas of the cutting tool and affect these areas.



**Figure 1.** Geometric parameters of cutting tool.

**Table 1.** Mechanical properties and chemical composition of AISI 316 austenic steel.

| Parameter | Value |
|---|---|
| Density (lbs/cm$^3$) | 0,29 |
| Brinell hardness (HB) | 149 |
| Tensile stress (MPa) | 205 |
| Elastic modulus (GPa) | 193 |
| Chemical composition (%) | C: 0,035 Mn: 2,0 P: 0,040 S: 0,03 Si: 0,75 Cr: 16-18 Ni: 10-15 |

Within the scope of the experimental studies carried out, CD and EAD processes were carried out. Experimental parameters are given in Table 2. During the EAD process, the workpieces were placed in sample holders in electrophoresis solution. 10 mm diameter, 30o helix angle, 118o tip angle, N type DIN 345 uncoated HSS tools were used as cutting tools. The geometric parameters of the cutting tool are given in Figure 1. The cutting tool was renewed in each experiment to clearly observe the wear that occurred. In the EAD process, SiC powder with a size of 0.5 nm was used as nanoparticles in solution. The solution used was 1/100 SiC and 99/100 pure water by weight. To create the electric field, the solution was connected to the cathode to make it negatively charged, and the cutting tool was connected to the anode tip to make it positively charged. A direct current power supply with 0-3 A and 0-30 V characteristics was used to create the coating medium. The solution parameters for which EAD will be used are given in Table 3. During the experiments, a CNC milling machine (Jetco 3 axis CNC-Chinese) was used to perform the drilling and a dynamometer (ME-SYSTEME-K3D160; Germany) was used to measure the thrust force. The data acquisition frequency for thrust force measurement was 1 kHz. In tool wear studies, the amount of wear was measured with an optical microscope (NIKON-ECLIPSE MA100; Japan). In addition, the impacts of machining methods and parameters on wear were analyzed in scanning electron microscopy (SEM) and their effects were examined in detail. To investigate the change of tool wear during drilling process, tool wear was measured by looking at the amount of wear at the end of 25 holes to analyze the effect of cutting speed, feed rate and machining methods on tool wear. The number of holes was selected as 25 because it was the optimum value for wear in the preliminary experiments. Each drill was measured twice to obtain accurate results. The experimental setup is given in Figure 2.
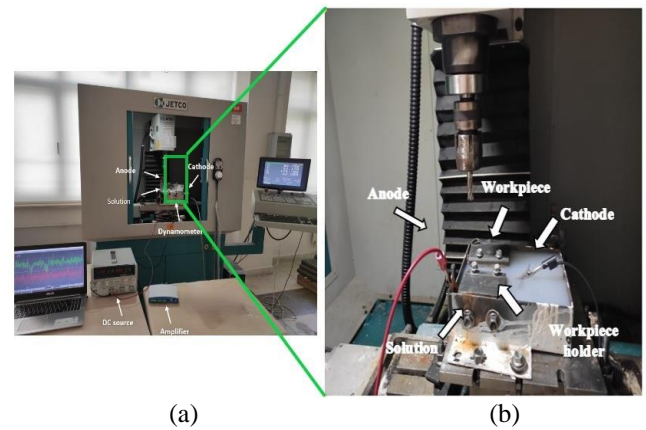


(a) (b)
**Figure 2.** a) Experimental setup b) Cutting area.

**Table 2.** Experimental parameters.

| Parameter | Conventional drilling | Electrophoresis assisted drilling |
|---|---|---|
| Spindle speed (m/min) | 20-30-40 | 20-30-40 |
| Feed rate (mm/dev) | 0,09-0,12-0,15 | 0,09-0,12-0,15 |
| Drilling diameter (mm) | 10 | 10 |
| Drilling cutting edge angle (degrees) | 35 | 35 |

**Table 3.** Electrophoresis solution parameters.

| Parameter | Value |
|---|---|
| Particle size (nm) | 0,5 |
| Particle type | Silicon carbide (SiC) |
| Applied voltage (DC)(V) | 10 |
| Working fluid | Pure water |

## 3 Results and Discussion

### 3.1 Tool Wear Results

Predicting tool wear is a difficult process because it is a parameter that changes over time in every manufacturing process. Workpieces produced with worn tools cause negative effects such as dimensional differences and poor surface quality [23]. Therefore, reducing tool wear has an important place in machining. Figure 3a shows the impacts of machining methods on wear and their changes depending on cutting speed. With increasing cutting speeds at fixed feed rate (0.12 mm/rev), cutting tool wear increased rapidly in both CD and EAD. As the number of revolutions increases, it causes more friction. As a result, it increases the temperature, creates corrosion mechanisms and increases wear [24]. When the cutting speed in CD increased from 20 m/min to 40 m/min, tool wear increased by 65%. Similarly, this rate was found to be 50% in EAD. Figure 3b shows the impacts of machining methods on wear and their changes depending on the feed rate. At fixed cutting speed (30 m/min), cutting tool wear increased in both machining methods as the feed rate increased from

0.09 mm/rev to 0.15 mm/rev. Tool wear increased as the amount of chip removed increased as the feed rate increased [23]. When the feed rate in CD increased from 0.09 mm/rev to 0.15 mm/min, tool wear increased by 41%. Similarly, in EAD this rate is 42%.
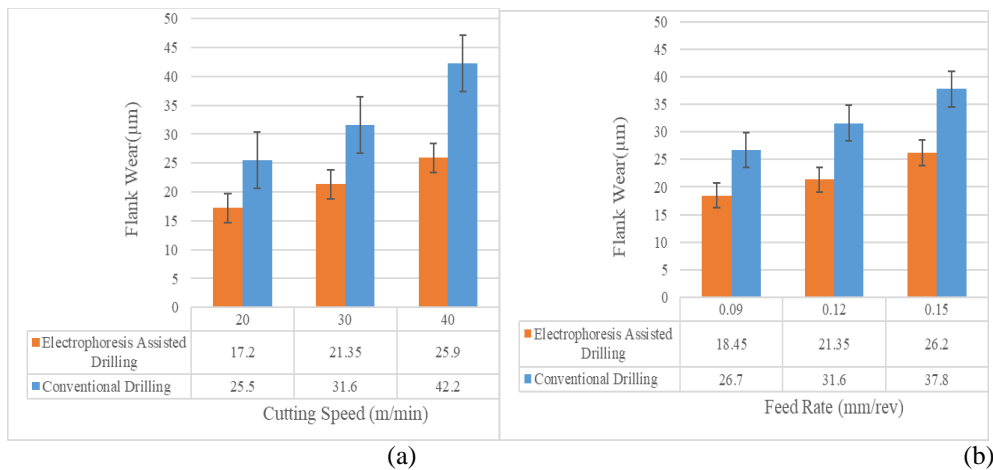


**Figure 3.** Flank wear values a) According to cutting speed, b) According to feed rate.

During the machining process, nanoparticles are attracted to the cutting tool due to the electromagnetic field generated by the chemical interactions of the nanoparticles in pure water. This phenomenon enables the coating of the cutting tool with SiC nanoparticles. Wear is reduced by attracting nanoparticles to the wear areas on the cutting tool while drilling and penetrating the worn areas. Additionally, the temperature decreased because the drilling process took place in the electrophoretic solution. The decrease in temperature minimized thermal softening and reduced wear compared to CD.

Figure 4a and 4b show SEM analysis images showing tool wear types at a cutting speed of 30 m/min and a feed rate of 0.15 mm/rev. Side wear was observed as a result of abrasive wear during processing with CD. In addition, notch wear and occasional tip fractures were observed in CD due to the adhesive wear mechanism caused by high pressure and temperature. Reduced side wear was observed due to EAD reducing the cutting temperature compared to CD. In addition, nanoparticles prevent wear mechanisms by penetrating the wear zones in the cutting tool.

The types of wear and tool damage that occurred on the cutting tools used in the experiments carried out at 40 m/min (max) cutting speed and 0.12 mm/rev feed rate by applying CD are shown in Figure 4c. Small fractures and flank wear occurred on the cutting tool at maximum cutting speed. Due to the increasing speed values, the effect of friction increases and an increase in flank wear occurs [25]. The types of cutting tool damage that occurred in the cutting tools used in the experiments carried out with CD at 30 m/min cutting speed and 0.15 mm/rev (max) feed rate are seen in Figure 4d. Flank wear, notch wear and fracture occurred at the maximum feed rates. The high cutting forces formed by the increase in feed rate create thermal and mechanical stresses in the cutting zone and thus fracture and flank wear occur [26].
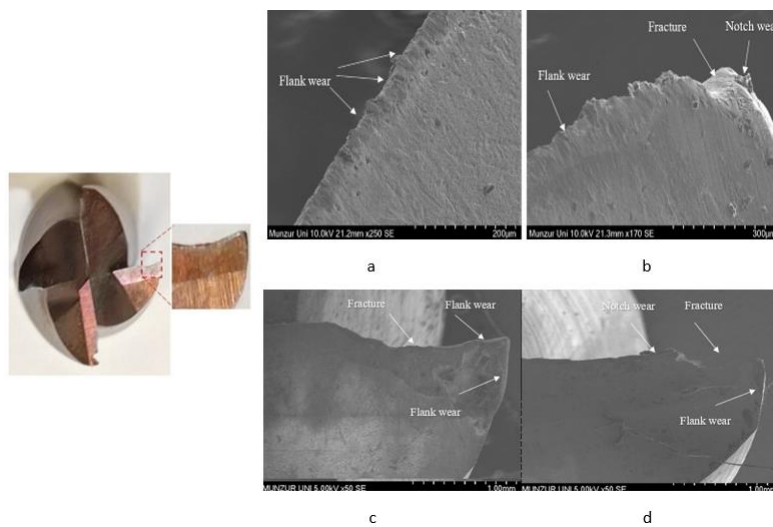


**Figure 4.** Wear on cutting tools a) Electrophoresis assisted drilling b) Conventional drilling c) Maximum cutting speed d) Maximum feed rate.

Figure 5a and Figure 5b show the EDS analysis of the cutting edge where the wear is the most at 30 m/min cutting speed and 0.12 mm/rev feed rate under EAD and CD machining conditions. The presence of elements such as Ni and Cr shown on the cutting edge in CD confirms that these elements move from the workpiece to the cutting tool. Thus, the workpiece sticks to the cutting tool [27]. In EAD machining, the presence of elements

belonging to the workpiece is seen in small amounts on the cutting tool. In EAD machining, the high amount of Si in the cutting area of the cutting tool proves that the abrasive particles move to the wear area of the cutting tool. During drilling, nano particles move to the worn areas with the help of the electric field and provide coverage of the area. This coating reduces wear on the cutting tool in EAD machining and causes flank wear.
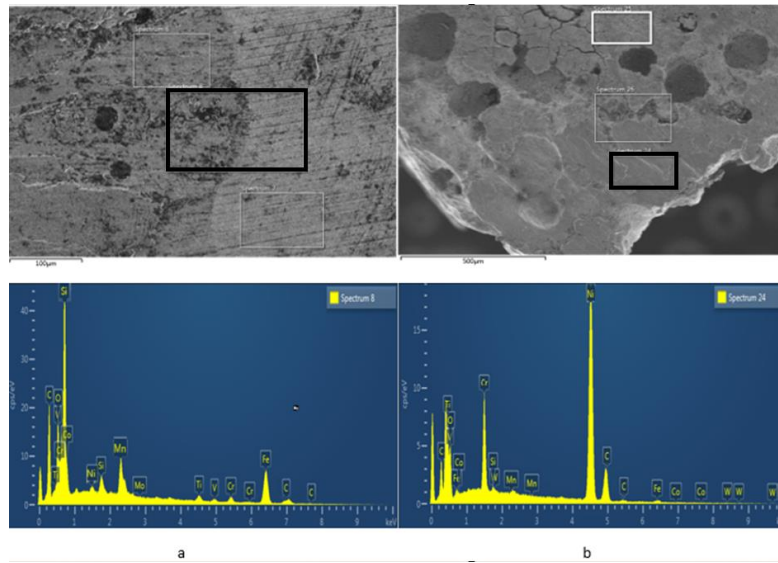


**Figure 5.** EDS results of cutting tool surface in a) EAD b)CD.

### 3.2 Thrust Force Results

Determination of thrust force is important to determine the power to be used in machining. Thrust forces ($F_z$) measured with the help of a dynamometer were taken as cutting forces. In Figure 5 and Figure 7, thrust forces ($F_z$) measured with the help of a dynamometer were taken as cutting forces; force signals and the change of thrust force values depending on cutting speed and feed rate are given in the processing of AISI 316 austenitic stainless steel with EAD and CD. Figure 6 shows real-time thrust force signals and thrust force values according to the change of cutting speed at a fixed feed rate of 0.12 mm/rev. According to experimental studies, both CD and EAD thrust decreased with increasing speed. Increasing the cutting speed in the cutting zone provides thermal softening. This reduces unwanted friction. Additionally, increased thermal softening has the effect of reducing workpiece hardness. For these reasons, increasing the cutting speed reduces the thrust force. When the thrust forces are examined according to the processing methods, the thrust force values obtained with EAD at all cutting speeds are lower than those with CD. The rationale behind this phenomenon is that in the EAD method, nanoparticles are able to penetrate the cutting tool due to the electromagnetic field, thereby preventing wear. Reducing tool wear reduces the force exerted when removing material from the workpiece [28]. At 30 m/min, the thrust force values obtained with EAD decreased by 18.51% compared to CD. While the maximum thrust force measured at CD was 73.5 N at 20 m/min, it was measured as 61.5 N at EAD.
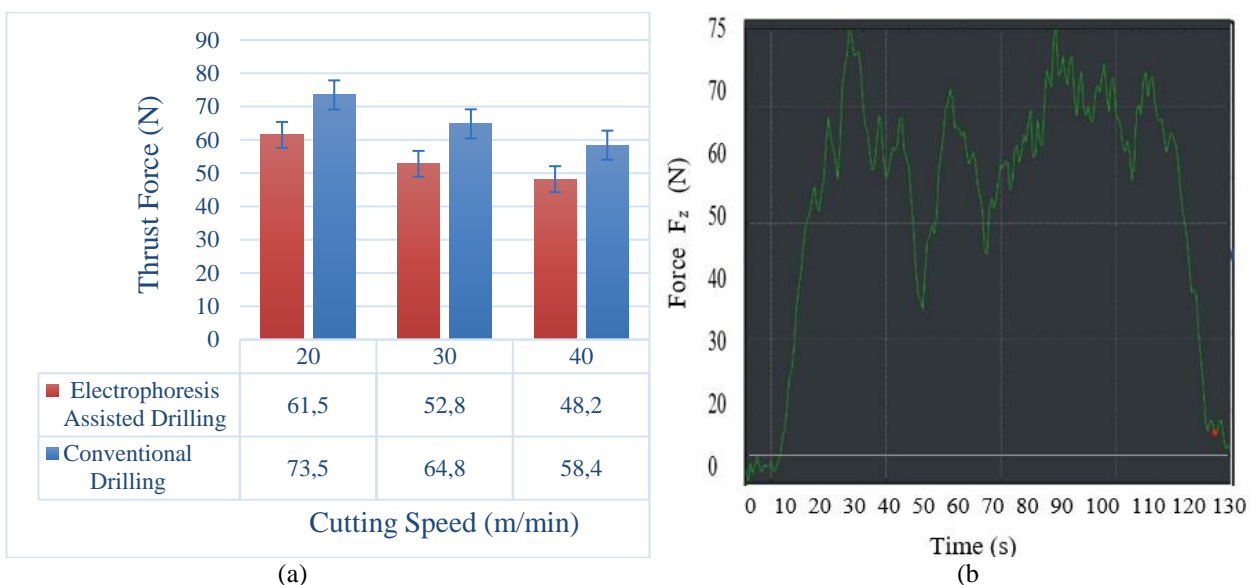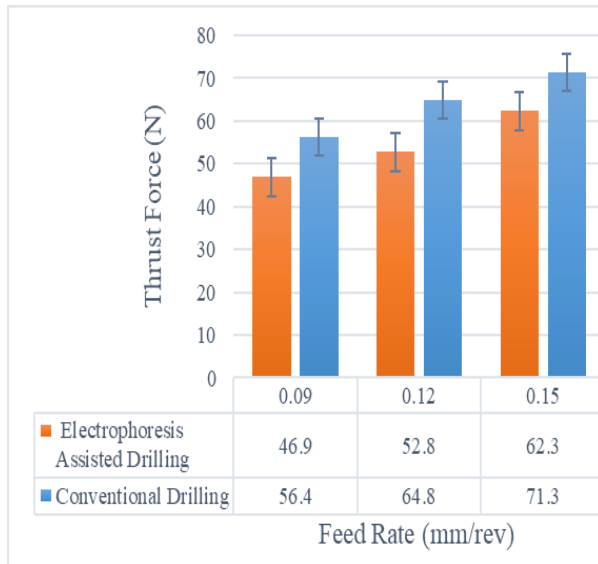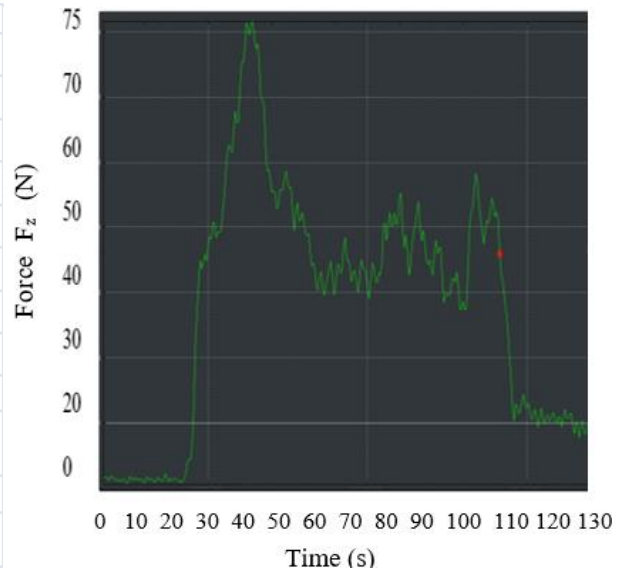


| Cutting Speed (m/min) | 20 | 30 | 40 |
|---|---|---|---|
| Electrophoresis Assisted Drilling | 61,5 | 52,8 | 48,2 |
| Conventional Drilling | 73,5 | 64,8 | 58,4 |

(a)      (b)

**Figure 6.** a) Effect of cutting speed on thrust force b) Thrust force signal.

In Figure 7, thrust force signals and thrust force values at variable feed rates at a fixed cutting speed of 30 m/min are given. In the two machining methods, the thrust force values are at their lowest at a feed rate of 0.09 mm/rev. As the feed rate increases, the amount of chip removed increases. Therefore, increasing the feed rate causes the thrust force to increase in both machining methods. Increasing the feed rate increases the amount of chip and increases the load on the tool. This causes more chip removal, thus increasing the thrust force [29]. When the thrust forces obtained at a feed rate of 0.15 mm/rev were examined, the thrust force measured by EAD decreased by approximately 12.62% compared to CD. While the maximum cutting force measured in CD was 71.3 N at a feed rate of 0.15 mm/rev, it was measured as 62.3 N at a feed rate of 0.15 mm/rev in EAD.




(a)                                                      (b)

**Figure 7.** a) Effect of feed rate on thrust force b) Thrust force signal.

## 4   Conclusion

As a result of experimental studies on CD and EAD of AISI 316L austenitic stainless steel with HSS cutting tools, the following conclusions can be drawn:

- When the cutting tool wear values are examined, tool wear values increased for both machining methods with the increase of cutting speed and feed rate. Tool wear values obtained with EAD were lower than those with CD. While side edge wear and notch wear were observed as wear types in CD, only side edge wear was observed in EAD. Tip breakage occurred in some places in the CD.

- Thrust force decreased for both machining methods due to increasing cutting speed at constant feed rate. In experiments conducted at variable cutting speeds, the maximum thrust force was measured as 73.5 N at CD at a cutting speed of 20 m/min. The lowest thrust force was measured as 48.2 N in EAD at a cutting speed of 40 m/min. At a cutting speed of 30 m/min, EAD reduced the thrust force by 18.51% compared to CD.

- Thrust force increased for both machining methods due to increasing feed rate at fixed cutting speed. At a fixed cutting speed of 30 m/min and varying feed rates, the highest thrust force was measured as 71.3 N at CD at a feed rate of 0.15 mm/rev. The lowest thrust force was measured as 46.8 N in EAD at a feed rate of 0.09 mm/rev. At a feed rate of 0.15 mm/rev, EAD reduced the thrust force by 12.62% compared to CD.

## Declaration

Ethics committee approval is not required.

## References

[1] Ankalagi, S., Gaitonde, V. N., & Petkar, P. (2017). Experimental Studies on Hole Quality in Drilling of SA182 Steel. *Materials Today: Proceedings, 4*(10), 11201-11209.

[2] Naves, V. T. G., Da Silva, M. B., & Da Silva, F. J. (2013). Evaluation of the Effect of Application of Cutting Fluid at High Pressure on Tool Wear During Turning Operation of AISI 316 Austenitic Stainless Steel. *Wear, 302*(1), 1201-1208.

[3] Pilkington, A., Dowey, S. J., Toton, J. T., & Doyle, E. D. (2013). Machining With AlCr-Oxinitride PVD Coated Cutting Tools. *Tribology International, 65,* 303-313.

[4] Kumar, C. S., Urbikain, G., Fernandes, F., AL Rjoub, A., & De Lacalle, L. N. L. (2024). Influence of V Concentration in TiAlSiVN Coating on Self-Lubrication, Friction and Tool Wear During Two-Pass Dry Turning of Austenitic Steel 316 L. *Tribology International, 193,* 109355.

[5] Pang, X., Zhang, B., Li, S., Zeng, Y., Liu, X., Shen, P., ... & Deng, W. (2022). Machining performance evaluation and tool wear analysis of dry cutting austenitic stainless steel with variable-length restricted contact tools. *Wear, 504,* 204423.

[6] Ağar, S., & Tosun, N. (2021). Ultrasonic assisted turning of AISI 52100 steel using nanoparticle-MQL method. *Surface Topography: Metrology and Properties, 9*(1), 015024.

[7] Sujan Kumar, M., & Deivanathan, R. (2021). Effect of Process Parameters on Drilling—An Overview. *Materials Today: Proceedings, 46,* 1401-1406.

[8] Samy, G. S., & Kumaran, S. T. (2017). Measurement and Analysis of Temperature, Thrust Force and Surface Roughness in Drilling of AA (6351)-B4C Composite. *Measurement, 103,* 1-9.

[9] Munaro, R., Attanasio, A., Abeni, A., Cappellini, C., Tavormina, P., & Venturelli, F. (2024). A New Architecture Paradigm for Tool Wear Prediction During AISI 9840 Drilling Operation. *Procedia Computer Science, 232,* 1617-1625.

[10] Vasumathy, D., & Meena, A. (2017). Influence of Micro Scale Textured Tools on Tribological Properties at Tool-Chip Interface in Turning AISI 316 Austenitic Stainless Steel. *Wear, 376-377,* 1747-1758.

[11] Kümmel, J., Braun, D., Gibmeier, J., Schneider, J., Greiner, C., Schulze, V., & Wanner, A. (2015). Study on micro texturing of uncoated cemented carbide cutting tools for wear improvement and built-up edge stabilisation. *Journal of Materials Processing Technology, 215*, 62-70.

[12] Jawahir, I. S., Brinksmeier, E., M'saoubi, R., Aspinwall, D. K., Outeiro, J. C., Meyer, D., ... & Jayal, A. D. (2011). Surface integrity in material removal processes: Recent advances. *CIRP annals, 60*(2), 603-626.

[13] Kümmel, J., Gibmeier, J., Müller, E., Schneider, R., Schulze, V., & Wanner, A. (2014). Detailed Analysis of Microstructure of Intentionally Formed Built-Up Edges for Improving Wear Behaviour in Dry Metal Cutting Process of Steel. *Wear, 311*(1), 21-30.

[14] Axinte, D. A., Andrews, P., Li, W., Gindy, N., Withers, P. J., & Childs, T. H. C. (2006). Turning of Advanced Ni-Based Alloys Obtained Via Powder Metallurgy Route. *CIRP Annals, 55*(1), 117-120.

[15] Yıldırım, Ç. V., Kıvak, T., Sarıkaya, M., & Erzincanlı, F. (2017). Determination of MQL Parameters Contributing to Sustainable Machining in the Milling of Nickel-Base Superalloy Waspaloy. *Arab Journal of Science and Engineering, 42*(11), 4667-4681.

[16] Ali, M. A. M., Azmi, A. I., Murad, M. N., Zain, M. Z. M., Khalil, A. N. M., & Shuaib, N. A. (2020). Roles of New Bio-Based Nanolubricants Towards Eco-Friendly and Improved Machinability of Inconel 718 Alloys. *Tribology International, 144,* 106106.

[17] Khan, M. M. A., Mithu, M. A. H., & Dhar, N. R. (2009). Effects of minimum quantity lubrication on turning AISI 9310 alloy steel using vegetable oil-based cutting fluid. *Journal of materials processing Technology*, 209(15-16), 5573-5583.

[18] Shokoohi, Y., Khosrojerdi, E., & Rassolian Shiadhi, B. H. (2015). Machining and Ecological Effects of a New Developed Cutting Fluid in Combination With Different Cooling Techniques on Turning Operation. *Journal of Cleaner Production, 94,* 330-339.

[19] Jindal, H., Kumar, S., & Kumar, R. (2020). Environmental Pollution and Its Impact on Public Health: A Critical Review. *TARCE, 9*(1), 11-18

[20] Lian, H. S., Guo, Z. N., Liu, J. W., Huang, Z. G., & He, J. F. (2016). Experimental Study of Electrophoretically Assisted Micro-Ultrasonic Machining. *International Journal of Advanced Manufacturing Technology, 85*(9), 2115-2124.

[21] He, J., Guo, Z., Lian, H., Wang, J., Chen, X., & Liu, J. (2020). Improving the Machining Quality of Micro Structures by Using Electrophoresis-Assisted Ultrasonic Micromilling Machining. *International Journal of Precision Engineering and Manufacturing-Green Technology, 7*(1), 151-161.

[22] Besra, L., & Liu, M. (2007). A Review on Fundamentals and Applications of Electrophoretic Deposition (EPD). *Progress in Materials Science, 52*(1), 1-61.

[23] Colantonio, L., Equeter, L., Dehombreux, P., & Ducobu, F. (2021). A Systematic Literature Review of Cutting Tool Wear Monitoring in Turning by Using Artificial Intelligence Techniques. *Machines, 9*(12), Article 12.

[24] Huang, W., Cao, S., Li, H. N., Zhou, Q., Wu, C., Zhu, D., & Zhuang, K. (2021). Tool wear in ultrasonic vibration–assisted drilling of CFRP: a comparison with conventional drilling. *The International Journal of Advanced Manufacturing Technology, 115*(5), 1809-1820.

[25] Dadgari, A., Huo, D., & Swailes, D. (2018). Investigation on tool wear and tool life prediction in micro-milling of Ti-6Al-4V. *Nanotechnology and Precision Engineering (NPE), 1*(4), 218-225.

[26] Hou, Y., Zhang, D., Wu, B., & Luo, M. (2014). Milling force modeling of worn tool and tool flank wear recognition in end milling. *IEEE/ASME Transactions on Mechatronics*, 20(3), 1024-1035.

[27] An, Q., Chen, J., Tao, Z., Ming, W., & Chen, M. (2020). Experimental investigation on tool wear characteristics of PVD and CVD coatings during face milling of Ti6242S and Ti-555 titanium alloys. *International Journal of Refractory Metals and Hard Materials, 86,* 105091.

[28] Subhedar, D. G., Chauhan, K. V., & Patel, D. A. (2022). An Experimental Investigation of TiN Coating on Cutting Force and Surface Finish in Milling of Aluminium. *Materials Today: Proceedings, 59,* 161-165.

[29] Ercetin, A., Aslantaş, K., Özgün, Ö., Perçin, M., & Chandrashekarappa, M. P. G. (2023). Optimization of Machining Parameters to Minimize Cutting Forces and Surface Roughness in Micro-Milling of Mg13Sn Alloy. *Micromachines, 14*(8), Article 8.

# INVESTIGATION OF THE USE OF NANOPARTICLES IN THERMAL INSULATION MATERIALS

*Ahmet Beyzade Demirpolat*[*1] iD *, Muhammed Mustafa Uyar*[2] iD

[1]*Malatya Turgut Özal University, Arapgir Vocational School, Department of Electronic Automation, 44800, Malatya, Turkey*
[2]*Malatya Turgut Özal University, Arapgir Vocational School, Department of Construction Machinery Operator, 44800, Malatya, Turkey*

## Abstract

*Original scientific paper*

Today, the concept of energy conservation has become a much more important concept due to the difficulty in accessing energy and the increasing cost of energy resources. The fact that fossil energy resources have started to be depleted in recent years worldwide has led mankind to renewable and sustainable energy resources. However, the fact that such resources are not yet at a level to meet the needs has shown the necessity of using energy economically. In our research, the thermal conductivities of the nanoparticles produced by us were determined in terms of evaluating the use of nanoparticle materials, which is a new perspective on energy saving, in thermal insulation materials. Then, the thermal conductivity coefficients of the nanoparticles in the literature were investigated and compared with the values of the nanoparticles produced by us, and the suitability of the use of the nanomaterials we produced in insulation materials was evaluated. In the study, the heat transfer coefficients of $Al_2O_3$ and CuO nanoparticles were found to be 34.2 and 65.4 W/mK, respectively. In the literature review, it was seen that these values were 36 and 65.8, respectively. As a result of the evaluations, it was observed that the CuO nanoparticle produced by us gave similar results with the literature, and the $Al_2O_3$ nanoparticle gave better results than similar studies at a rate of 5%.

*Keywords: Nanoparticles, thermal insulation, energy saving.*

# NANOPARÇACIKLARIN ISI YALITIM MALZEMELERİNDE KULLANIMININ İNCELENMESİ

## *Özet*

*Orijinal bilimsel makale*

Günümüzde enerjiye ulaşımın zorlaşması ve enerji kaynaklarının giderek pahalılaşmasından dolayı, enerji tasarrufu kavramı çok daha önemli bir kavram haline gelmiştir. Dünya genelinde son yıllarda fosil enerji kaynaklarının tükenmeye başlamış olması, insanoğlunu yenilenebilir ve sürdürülebilir enerji kaynaklarına yönlendirmiştir. Fakat bu tür kaynaklarda henüz ihtiyaca cevap verecek düzeyde olmayışı, enerjiyi tasarruflu bir şekilde kullanmanın gerekliliğini göstermiştir.
Araştırmamızda enerji tasarrufu konusunda yeni bir bakış açısı olan nanopartikül malzemelerin ısı yalıtım malzemelerinde kullanılmasının değerlendirilmesi yönünden hem tarafımızca üretilmiş olan nanopartiküllerin ısıl iletkenlikleri tespit edilmiştir. Daha sonra literatürdeki nanopartiküllerin ısı iletim katsayıları araştırılıp tarafımızca üretilmiş olan nanopartiküllerin değerleri ile karşılaştırma yapılarak, yalıtım malzemelerinde üretmiş olduğumuz nanomalzemelerin kullanımının uygunluğu değerlendirmelere tabi tutulmuştur. Çalışmada, $Al_2O_3$ ve CuO nanopartiküllerinin ısı transfer katsayıları sırasıyla 34.2 ve 65.4 W/mK olarak bulunmuştur. Literatür taramasında bu değerlerin sırasıyla 36 ve 65.8 olduğu görülmüştür. Değerlendirmeler sonucunda tarafımızca üretilmiş olan CuO nanopartikülünün literatürle benzer sonuçlar verdiği görülmüş olup $Al_2O_3$ nanopartikülünün ise %5 oranında benzer çalışmalara göre daha iyi sonuç verdiği gözlemlenmiştir.

*Anahtar Kelimeler: Nanopartikül, ısı yalıtımı, enerji tasarrufu.*

## 1 Introduction

With the developing technology, it has become easier for human beings to access energy resources. This has led to an increase in energy consumption and new research on the efficient use of resources. Due to the climate crisis and drought caused by global warming, the amount of energy produced from hydroelectric power plants and wind power plants has decreased significantly. This situation has led to an increase in the use of fossil fuels, one of the most traditional methods of energy production, and the inability to meet the energy demand due to the decrease in resources. There has been a significant increase in the use of renewable energy sources in Turkey. However, this increase still has a small share in the energy used. According to the reports of the Turkish Electricity

Transmission Company (TETC), the share of wind and solar energy in total energy production is 12 percent, while the share of hydroelectric energy production in total consumption is 25.6 percent [1]. As can be understood from the published report, most of the energy production in Turkey is still provided by fossil fuels, and in case the demand cannot be met, exports are resorted to. According to a report by Anatolia Agency, in the first quarter of 2021, Turkey's energy imports increased by 9.6 percent compared to the same period last year and amounted to 61 billion dollars [2]. Another problem caused by fossil fuels is air pollution. In the report published by the Right to Clean Air Platform, it is stated that air pollution has caused more than six times more deaths than traffic accidents every year since 2017, and Istanbul has been the city with the highest number of deaths due to air pollution since 2017 [3]. For these reasons, it is important to take energy saving measures in Turkey in order to reduce deaths due to air pollution, to reduce the share of energy imports and to use resources efficiently. The simplest definition of a nanoparticle is a particle on a very small scale. The nanoscale defines the range of 1-100 nm. The basis on which nanotechnology is focused on is defined by the American National Nanotechnology Initiative as "the essence of nanotechnology is the ability to work at the molecular level, atom by atom structuring, basically creating large structures with new molecular arrangements". Nano materials are a general name given to materials used in nanotechnology. Nano materials science is the branch of science that studies how materials behave at the nano level. The high area-to-volume ratio of nano materials opens the door to new applications. This is also known as the quantum effect. This also affects biomaterial applications. With the quantum effect, the size of particles decreases and the electronic properties of materials change; various metal, semiconductor and insulator nanomaterials gain importance with this change in their mechanical, magnetic, optical and chemical properties. The physical properties of materials reduced to nano size change. Nano technology is the development of new materials, systems and devices using these unusual properties of materials. In other words, there are two important goals underlying nanotechnology. The first is to utilize the different properties of nano materials developed by using special production techniques, and the second is to change the internal structure of large-scale materials at the atomic level in a controlled manner and thus to give them extraordinary properties [4]. The main reason for heat loss in buildings is that heat wants to pass from a high-temperature environment to a low-temperature environment. According to the report of the Chamber of Mechanical Engineers, the thermal comfort condition is 50 percent relative humidity and indoor temperature ranging between 20-25 °C [5]. If the interior surface temperature is 5-6 °C different from the space temperature, a thermal bridge is formed on the building surface. Columns, beams, beams, curtain concrete and slabs that form heat bridges in buildings cause heat loss up to 20-50 percent on the outer surface of the building. The reason for such a high percentage is that the thermal conductivity of reinforced concrete has a high value of 2.1 W/mK. Another problem caused by thermal bridges is condensation. Condensation causes paint and plaster

flaking, fungus and mold on the inner and outer surfaces of the wall. The reason for condensation is that the partial pressure due to temperature causes vapor transmission due to the difference between the indoor and outdoor environment. Condensation occurs due to the incompatibility between the thermal conductivity and vapor diffusion resistance values of the materials forming the wall. Thermal insulation is a system designed to minimize heat exchange between one region and another. Thus, the formation of thermal bridges and condensation can be minimized and a comfortable life can be ensured in buildings. Nanostructured materials such as nanoparticles, nanowires and nanolaminates have attracted great interest in applications in many fields due to their large specific surface areas and extraordinary physical properties. In the theoretical studies first carried out by Phaser, it was found that the thermal contact resistances between nanoparticle particles were high. For this reason, it was concluded that the thermal conductivity of nanoparticle beds may be lower than the minimum thermal conductivity in the Einstein limit. The low thermal conductivity of a material is related to its low heat conductivity. It is preferred that the thermal conductivity of thermal insulation materials is close to zero. In other words, the lower the thermal conductivity, the better the thermal insulation performance of the material [6]. These ultra-low thermal conductivities in nanoparticle beds were observed in experimental studies conducted by Hu et al. In this study, commercially available nanoparticles with nominal particle sizes of 300 and 500 nm were used. Alumina nanoparticle samples were pressed with the help of stainless steel rods. The thermal conductivity of the particle bed was measured with a heat conduction apparatus. The purpose of choosing steel rods is to increase the precision of the measurement. In the tests, the temperature of the adjacent thermocouple was measured around 1-2 °C and the precision was +-0.2 °C. The thermal conductivity of the packed alumina nanoparticle bed was measured to be 0.035W/mK. This value is only 35 percent higher than the thermal conductivity of air and smaller than the lowest thermal conductivity of tungsten diselenide (WeS$_2$), the most widely used thermal insulation material. This suggests that alumina nanoparticle beds would be suitable for high-temperature thermal insulation and energy conversion applications. In addition, since nanoparticle beds are insensitive to external pressure, they have low thermal conductivity even at high pressure [7]. Mishra et al. aimed to produce thermal insulation material from oxide nanoparticles. As a result of the experiments, it was concluded that oxide nanoparticles can be limited by low melting points at high temperature. As a result of using silica and alumina nanoparticle beds together, it has been observed and reported that the phase transformation of alumina will occur at a temperature lower than 1200 °C and the structure shrinkage of silica will start at a temperature lower than 1000 °C. The fact that phase transformation and structure shrinkage occur at such high temperatures is an important indicator that the silica and alumina nanoparticles used can be used in thermal insulation materials [8]. According to the studies conducted by Wu et al., oxide nanoparticles can be used in thermal insulation materials due to their low thermal reliability at

high temperatures. Firstly, silicon carbide powders were compacted in a powder compaction machine to form a cylindrical nanoparticle bed. In the formation of the beds, different pressures such as 2,4,6,6,8,8,10,12 and 15 MPa were applied to obtain multiple different pore structures. Six of each sample were prepared to obtain an average conductive value for each pressure value. The samples were heated in a vacuum tube furnace, increasing the temperature by 10 K/min each time. Thermal conductivities at different temperatures were measured with the help of a special device. By this process, the thermal conductivity, phase transformation temperature, radiation heat transfer and convection heat transfer of the nanoparticle beds produced were found. In the light of these data, it was reported that SiC has a thermal conductivity of less than 0.07 W/mK and can be an excellent thermal insulation material. It was also observed that Silicon Carbide (SiC) retains its morphology up to 1800 C due to its thermal contact resistance at high temperatures and can resist up to 2000 °C without phase transformation [9]. In the study by Kuşkonmaz, the conditions required to produce high density $Al_2O_3$ at high pressure and different sintering temperatures were investigated. The starting powder used to produce the nanoparticle bed was selected as 20nm on average. The starting powder was heated at 700 °C for three hours to lose its binding properties. Then, $Al_2O_3$ powder without any additives was cold pressed by applying 20 mPa pressure and samples with a diameter of 20 mm and a height of 10 mm were obtained. To prevent grain growth, 10 percent of the weight of $TiO_2$ was added to each sample by sol-gel method. Phase analysis of the sintered samples was performed by X-ray diffraction and grain sizes were estimated from high-resolution scanning electron micrographs. Microhardness was determined on polished surfaces by applying load to the samples.

As a result of these studies,

- Effect of applied pressure duration on phase transformation,
- All sintered samples showed the presence of α phase without evidence of γ phase.
- It was also determined that under the applied pressure and temperature, the sintering time had no significant effect on the phase content [10].

These studies with alumina silica and carbon nanoparticles show that nanoparticles can be used in thermal insulation due to their high thermal resistance. One of the most important factors of heat losses is the gaps in the carrier systems. According to the Guidelines for the Imaging of Building Heat Losses with Thermal Camera published by the Ministry of Environment and Urbanization, heat losses in buildings monitored with thermal camera are shown in Figure 1. Close-up thermal imagery provides the necessary information about the structure of the walls and heat loss. As seen in Figure 1, heat losses from windows can be detected with digital systems. Necessary measures are taken in line with these determinations.


**Figure1.** Heat Loss through Window Openings [11].

In the study by Ning Li et al., nano antimony (flame retardant) doped tin oxide (ATO) was synthesized by sol gel method and nanoparticles were produced. The zeta potential (intergranular repulsion or attraction value), dispersant and pH values affecting the stability of the produced nanoparticles were evaluated. Antimony doped tin oxide (ATO) suspension with high stability was prepared and it was observed that pH value, dispersant type and dosage have a significant effect on the stability of ATO suspensions. For example, an ATO suspension with pH= 6-10 has a higher zeta potential and better stability. The study also indicated that among various dispersants, the stability of ATO suspension using poly acrylamide and sodium polyphosphate can be significantly improved and it is a reliable method to prepare stable suspensions of ATO nanoparticles for heat insulating glass paint [12]. Wu et al. investigated the addition of $SiO_2$ nanoparticles as an additive to insulation material. In addition to the addition of $SiO_2$ nanoparticles, they also added sawdust to the insulation material. They achieved a 15% decrease in density value with the addition of $SiO_2$ nanoparticles and 20% sawdust in the insulation material. They also concluded that it offers significant contributions with a 22% decrease in thermal conductivity [13]. Liu et al. investigated Silica aerogel used as insulation material in buildings. They investigated the contribution of nanoparticle additives such as $SiO_2$ and SiC to thermal conductivity values. They concluded that fiber-reinforced aerogel composites contribute to the thermal conductivity at high temperature [14].

Studies on thermal insulation applied to glass have revealed the necessity to find more transparent thermal insulation materials with the correct thermal insulation. Making maximum use of sunlight is at least as important for energy saving as proper thermal insulation. In their study, Ran et al. worked to further improve the transparent thermal insulation of $Cs_xWO_3$, which is frequently used in window glass with higher visible transmittance, near-infrared capability and energy saving due to its thermal stability. A controllable synthesis of $Cs_xWO_3$ nanoparticles was realized by solvothermal method from $Na_2WO_3.2H_2O$ and $Cs_2SO_4$, which are inexpensive and environmentally friendly. The reducibility and reduction mechanisms of citric acid, tartaric acid and oxalic acid were investigated. It was confirmed that tartaric acid has the strongest reducibility and can produce the most W5+ and oxygen vacancies in the production of $Cs_xWO_3$ before heat treatment.

After heat treatment, $Cs_xWO_3$ nanoparticles exhibited the best crystallinity and the visible light transmission was found to be about 10 percent higher than tartaric acid and citric acid [15]. In our research, the thermal conductivities

of the nanoparticles produced by us were determined in terms of evaluating the use of nanoparticle materials, which is a new perspective on energy saving, in thermal insulation materials. Then, the thermal conductivity coefficients of the nanoparticles in the literature were investigated and compared with the values of the nanoparticles produced by us, and the suitability of the use of the nanomaterials we produced in insulation materials was evaluated. In the study, the heat transfer coefficients of $Al_2O_3$ and CuO nanoparticles were found to be 34.2 and 65.4 W/mK, respectively. In the literature review, it was seen that these values were 36 and 65.8, respectively. As a result of the evaluations, it was observed that the CuO nanoparticle produced by us gave similar results with the literature, and the $Al_2O_3$ nanoparticle gave better results than similar studies at a rate of 5%.

## 2 Materials and Methods

### 2.1 Materials and Tools Used in Nano Particle Production

### 2.1.1 Materials Used in Particle Production

Aluminum Acetate, Copper Acetate, Sodium hydroxide, Ammonia, Pure Water were used in the content of nanoparticles produced by us under laboratory conditions.

### 2.1.2 Electronic Precision Weighing

The electronic precision balance used to adjust the material quantities is given in Figure 2.



**Figure 2.** Electronic precision scale.

### 2.1.3 Electronic Fish Mixer

The electronic fish mixer with speed and temperature settings is shown in Figure 3.
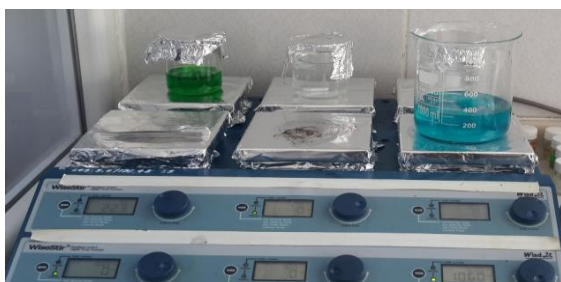


**Figure 3.** Electronic fish mixer.

### 2.1.4 Ultrasonic Bath

The ultrasonic bath with temperature and time adjustment features is shown in Figure 4.



**Figure 4.** Ultrasonic bath.

### 2.1.5 Beaker and Funnel

The beaker and funnel used to separate the pure water from the particles before drying to obtain the nanoparticles are given in Figure 5.



**Figure 5.** Beaker and Funnel.

### 2.1.6 High Temperature Regulated Oven

The high temperature regulated oven used to dry the particles at high temperature is shown in Figure 6.



**Figure 6.** High temperature regulated oven.

### 2.2 SEM Device Preparation Unit (Coating)

The material to be examined in the SEM device is made ready by coating. The SEM device preparation unit is given in Figure 7.
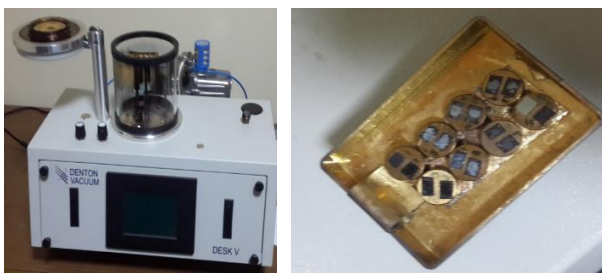
**Figure 7.** High temperature regulated oven.

## 2.3 SEM Device

Scanning Electron Microscope (SEM), which is produced in line with electrooptic principles, is one of the devices that serve the purpose of whether the particles are nanoparticles or not. In addition to its use in research and development studies in many fields, Scanning Electron Microscope is frequently used in chip production in microelectronics, error analysis in different branches of industry, biological sciences, medicine and criminal applications. The SEM device is given in Figure 8.



**Figure 8.** SEM device.

The materials for the production of $Al_2O_3$ and CuO nanoparticles were prepared in the following proportions. For the production of $Al_2O_3$ 10.8 grams (0.1 mol) aluminum and CuO nanoparticles, first 8.5 grams (0.1 mol) $Al_2O_3$ and copper acetate are dissolved in 500 ml ethanol for 30 minutes in an ultrasonic bath. Then 40 grams (1 mol) NaOH (sodium hydroxide) dissolves in 200 ml distilled water for 30 minutes in an ultrasonic bath. Finally, these mixtures are combined and stirred in a fish mixer for 1 hour. Then ammonia was added to the mixture in 50 ml beakers to obtain the mixture at various pHs. pH ratios were obtained. After the mixture was prepared, it was left to precipitate for 20 hours. At the end of the waiting process, filter paper was placed and after filtering in funnels, the material was subjected to drying at 50 ºC. Finally, after the material was heat treated at 470 ºC for 1 hour, our material was ready. For this reason, there are parameters that are important in the synthesis process when producing particles. These parameters are the material ratios used, the reaction time in the fish mixer in terms of homogeneity of the solution and the heat treatment time to which the material is subjected. As a result of the analysis of the nanoparticles produced in our study, the accuracy of the mentioned parameters was observed as it was seen that the production was successfully realized.

## 2.4. SEM Images of Materials

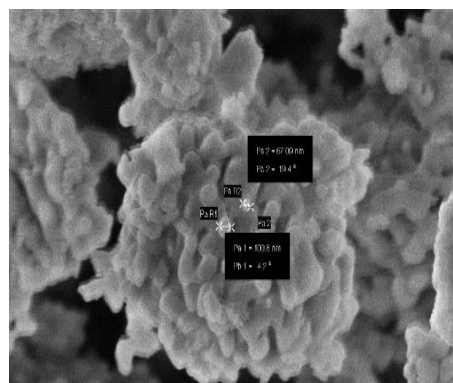SEM images of the nanoparticle types produced are given in Figure 9 and Figure 10.



**Figure 9.** SEM image of $Al_2O_3$.



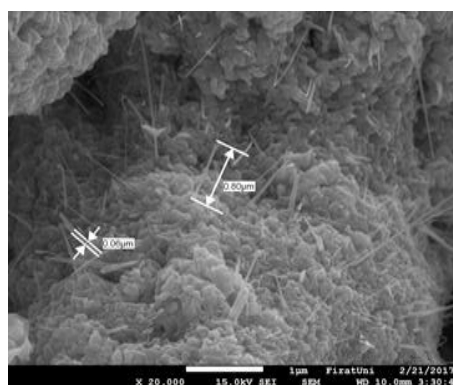**Figure 10.** SEM image of CuO.

SEM analysis showed that the nanoparticles produced were successful.

## 2.5. Thermal Conductivity Measurements of Nanoparticles

Thermal conductivity measurements were performed after nanoparticle production. TLS-100 thermal conductivity measurement device was used for thermal conductivity determinations. Knowing the thermal properties of materials is very important in achieving optimum performance where the material is used. Thermal conductivity is one of the most important thermophysical properties used to define the heat transport properties of materials. With the thermal conductivity analyzer, the thermal conductivity constant values (k) of materials can be determined in W/mK. The surface of the material is brought into contact with the sensor of the device and the thermal conductivity coefficient of the material is determined from the temperature interaction between the sensor and the sample. The schematic image of the device used is shown in Figure 11.



**Figure 11.** TLS-100 Thermal conductivity meter.

The thermal conductivity coefficients of the $Al_2O_3$ and CuO nanoparticles we produced were determined using the TLS-100 thermal conductivity meter. The uncertainty of the measuring instrument used is less than 5%. The heat transfer coefficients are given in Figure 12.
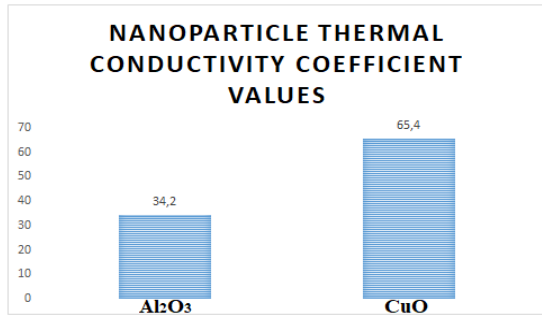


**Figure 12.** Heat Transmission Coefficients (W/mK) of the metal oxide types produced.

The nanoparticle types for which conductivity measurements were completed were compared with the literature. The nanoparticle types observed in the literature are given in Figure 13 [16].
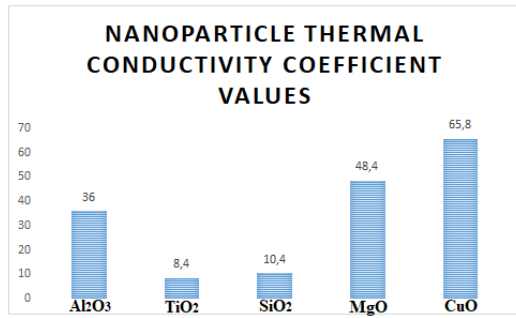


**Figure 13.** Heat Transmission Coefficients of metal oxide types in literature (W/mK).

## 3 Conclusion

As a result of the studies examined, it was understood that the use of nanoparticulate materials in the field of thermal insulation can make great contributions to energy saving, as well as having great economic benefits due to the lower cost of nanoparticles and the possibility of more production at low cost. Nanoparticles, which are easy to produce, transport and reach the desired properties due to their structure, have been a type of material that has attracted the attention of the whole world and has been the subject of many studies with its energy saving during the production phase, being economical and saving time by shortening the production time. In our research, the thermal conductivities of the nanoparticles produced by us were determined in terms of evaluating the use of nanoparticle materials, which are a new perspective on energy saving, in thermal insulation materials. Then, the thermal conductivity coefficients of the nanoparticles in the literature were investigated and compared with the values of the nanoparticles produced by us, and the suitability of the use of the nanomaterials we produced in insulation materials was evaluated. In the study, the heat transfer coefficients of $Al_2O_3$ and CuO nanoparticles were found to be 34.2 and 65.4 W/mK, respectively. In the literature review, it was seen that these values were 36 and 65.8, respectively. As a result of the evaluations, it was observed that the CuO nanoparticle produced by us gave similar results with the literature, and the $Al_2O_3$ nanoparticle gave better results than similar studies at a rate of 5%. The synthesis of nanoparticles produced under laboratory conditions involves a long and challenging process. In the age of developing and rapidly growing technology, it is seen that particle production is progressing day by day. In the coming years, it is thought that industrial mass production will be started as the fruit of scientific research.

## Declaration

Ethics committee approval is not required.

## References

[1] Türkiye Elektrik İletim Anonim Şirketi. (2021, 8 Kasım). *TEİAŞ*. Retrieved 8 November 2021 from https://www.teias.gov.tr/tr-TR/

[2] Anadolu Ajansı. (2021, 8 Kasım). *Türkiye'nin enerji ithalatı faturası ilk çeyrekte yüzde 13 azaldı*. Retrieved 8 November 2021 from https://www.aa.com.tr/tr/ekonomi/turkiyenin-enerji-ithalati-faturasi-ilk-ceyrekte-yuzde-13-azaldi/2230017

[3] Temiz Hava Hakkı Platformu. (2021, 8 Kasım). *Temiz Hava Hakkı*. Retrieved 8 November 2021 from https://www.temizhavahakki.com/kararrapor2020/?gclid=Cj0KCQiAsqOMBhDFARIsAFBTN3ezzx6MZ4rUt0wdunfktXyz1RjT9PGkAfRZi5Uz_oM0Dh6pxhkU6T8aAr24EALw_wcB

[4] Callister, W., & Rethwisch, D. (2013). *Materials Science and Engineering* (Cilt Eight Editions).

[5] Coşkun, C., Oktay, Z., & Ertürk, M. (2010). Konutların ısıtma sezonunda seçilen iç ortam sıcaklık parametresinin enerji-maliyet-çevre açısından değerlendirilmesi ve bir uygulama örneği. İstanbul: Makine Mühendisleri Odası.

[6] Phaser, R. (2006). Ultralow Thermal Conductivity Of A Packed Bed Of Crystalline Nanoparticles: A Theoretical Study. *Physical Review B, 74*.

[7] Hu, X., Prasher, R., & Lofgreen, K. (2007). Ultralow Thermal Conductivity Of Nanoparticle Packed Bed. *Applied Physics Letters, 91*.

[8] Mishra, R., Lesher, C., & Mukherjee, A. (1996). High-Pressure Sintering Of Nanocrystalline γAl2O3. *Journal Of The American Ceramic Society, 2989-2992*.

[9] Wu, D., & Huang, C. (2020). Thermal Conductivity Study Of SiC Nanoparticle Beds For Thermal Insulation Applications. *Physica E: Low-Dimensional Systems And Nanostructures, 118*.

[10] Kuşkonmaz, N. (2013). High Pressure Sintering Of Nano-Size γ-Al2O3. *Sintering Applications, Chapter 3*.

[11] Li, N., Meng, Q., & Zhang, N. (2014). Dispersion Stabilization Of Antimony-Doped Tin Oxide (ATO) Nanoparticles Used For Energy-Efficient Glass Coating. *Particuology, 49-53*.

[12] Ran, S., Liu, J., Shi, F., Fan, C., Yang, J., Chen, B., & Liu, S. H. (2019). Microstructure Regulation Of CsxWO3 Nanoparticles By Organic Acid For Improved Transparent Thermal Insulation Performance. *Materials Research Bulletin, 273-280*.

[13] Şahin, F., & Namlı, L. (2018). Nanoakışkanlarda Kararlılığın Isı Transferini İyileştirme Açısından Önemi. *Niğde Ömer Halisdemir Üniversitesi Mühendislik Bilimleri Dergisi, 7*(2), 880-898.